The geodynamic significance of UHP exhumation: New constraints from Tso Morari Complex, NW Himalaya

Anna Bidgood[1], Andrew J Parsons[2], Nicholas M W Roberts[3], David Waters[4], Simon Tapster[5], and Phillip Gopon[6]

[1]Carnegie Institution for Science
[2]University of Plymouth
[3]NERC Isotope Geosciences Laboratory
[4]Oxford University
[5]British Geological Survey
[6]University of Leoben

March 05, 2024

Abstract

The burial and exhumation of continental crust to and from ultrahigh-pressure (UHP) is an important orogenic process, often interpreted with respect to the onset and/or subduction dynamics of continent-continent collision. Here, we investigate the timing and significance of UHP metamorphism and exhumation of the Tso Morari complex, North-West Himalaya. We present new petrochronological analyses of mafic eclogites and their host-rock gneisses, combining U-Pb zircon, rutile and xenotime geochronology (high-precision CA-ID-TIMS and high-spatial resolution LA-ICP-MS), garnet element maps, and petrographic observations. Zircon from mafic eclogite have a CA-ID-TIMS age of 46.91 $\pm$ 0.07 Ma, with REE profiles indicative of growth at eclogite facies conditions. Those ages overlap with zircon rim ages (48.9 $\pm$ 1.2 Ma, LA-ICP-MS) and xenotime ages (47.4 $\pm$ 1.4 Ma; LA-ICP-MS) from the hosting Puga gneiss, which grew during breakdown of UHP garnet rims. We argue that peak zircon growth at 47-46 Ma corresponds to the onset of exhumation from UHP conditions. Subsequent exhumation through the rutile closure temperature, is constrained by new dates of 40.4 $\pm$ 1.7 and 36.3 $\pm$ 3.8 Ma (LA-ICP-MS). Overlapping ages from Kaghan imply a coeval time-frame for the onset of UHP exhumation across the NW Himalaya. Furthermore, our regional synthesis demonstrates a causative link between changes in the subduction dynamics of the India-Asia collision zone at 47-46 Ma and the resulting mid-Eocene plate network reorganization. The onset of UHP exhumation therefore provides a tightly constrained time-stamp significant geodynamic shifts within the orogen and wider plate network.

Abstract content goes here

Hosted file

Supporting Information 2_EPMA.xlsx available at https://authorea.com/users/633209/articles/651706-the-geodynamic-significance-of-uhp-exhumation-new-constraints-from-tso-morari-complex-nw-himalaya

Hosted file

Copy of Supporting Information 3_2_NR_031023.xlsx available at https://authorea.com/users/633209/articles/651706-the-geodynamic-significance-of-uhp-exhumation-new-constraints-from-tso-morari-complex-nw-himalaya

1   **The geodynamic significance of continental UHP exhumation: New constraints from the**

2   **Tso Morari Complex, NW Himalaya**

3

4   **Anna K. Bidgood[1], Andrew J. Parsons[2], Nick M W Roberts[3], , Dave Waters[1,4], Simon**

5   **Tapster[2], Phillip Gopon[5]**

6

7   [1] Department of Earth Sciences, University of Oxford, OX1 3AN, UK

8   [2] School of Geography, Earth and Environmental Sciences, University of Plymouth, PL4 8AA

9   [3] Geochronology and Tracers Facility, British Geological Survey, Nottingham, NG12 5GG, UK

10   [4] Museum of Natural History, University of Oxford, OX1 3PW, UK

11   [5] Dept. of Applied Geosciences and Geophysics, Montanuniversität Leoben, 8700, AT

12

13   AKB ORCID: 0000-0001-7750-9524

14   AJP ORCID: 0000-0001-7538-9418

15   NMWR ORCID: 0000-0001-8272-5432

16   DJW ORCID: 0000-0001-9105-9953

17   ST ORCID: 0000-0001-9049-0485

18   PG ORCHID: 0000-0003-3355-4416

19

20   *Correspondence (akbidgood@gmail.com)

21   **Key Points**

22   1. Geochronological constraints from the Tso Morari dome place the onset of exhumation from

23   ultrahigh-pressure conditions at 46.91 ± 0.07 Ma

24   2. Close correspondence to other ultrahigh-pressure ages imply a similar time-frame for the onset of

25   UHP exhumation across the NW Himalaya

26   3. The onset of UHP exhumation at 47-46 Ma timestamps geodynamic changes in the India-Asia

27   collision zone, which triggered an Eocene plate network reorganisation

28   **Abstract**

29   The burial and exhumation of continental crust to and from ultrahigh-pressure (UHP) is an important

30   orogenic process, often interpreted with respect to the onset and/or subduction dynamics of continent-

31   continent collision. Here, we investigate the timing and significance of UHP metamorphism and

32   exhumation of the Tso Morari complex, North-West Himalaya. We present new petrochronological

33   analyses of mafic eclogites and their host-rock gneisses, combining U-Pb zircon, rutile and xenotime

geochronology (high-precision CA-ID-TIMS and high-spatial resolution LA-ICP-MS), garnet element maps, and petrographic observations. Zircon from mafic eclogite have a CA-ID-TIMS age of 46.91 ± 0.07 Ma, with REE profiles indicative of growth at eclogite facies conditions. Those ages overlap with zircon rim ages (48.9 ± 1.2 Ma, LA-ICP-MS) and xenotime ages (47.4 ± 1.4 Ma; LA-ICP-MS) from the hosting Puga gneiss, which grew during breakdown of UHP garnet rims. We argue that peak zircon growth at 47-46 Ma corresponds to the onset of exhumation from UHP conditions. Subsequent exhumation through the rutile closure temperature, is constrained by new dates of 40.4 ± 1.7 and 36.3 ± 3.8 Ma (LA-ICP-MS). Overlapping ages from Kaghan imply a coeval time-frame for the onset of UHP exhumation across the NW Himalaya. Furthermore, our regional synthesis demonstrates a causative link between changes in the subduction dynamics of the India-Asia collision zone at 47-46 Ma and the resulting mid-Eocene plate network reorganization. The onset of UHP exhumation therefore provides a tightly constrained time-stamp significant geodynamic shifts within the orogen and wider plate network.

Key words: U-Pb geochronology; Himalayan Orogeny; eclogite; UHP metamorphism; continental collision; subduction-exhumation

1. Introduction

The exhumation of continental crust from ultra-high pressure (*hereafter referred to as "UHP exhumation"*) is an important yet poorly constrained orogenic process (Guillot et al., 2009, Hacker and Gerya, 2013, Warren, 2013). Many studies relate UHP exhumation to other orogenic processes such as a reduction in the slab-pull force during the subduction of continental crust, slab break-off, and/or onset of various modes of orogenic extension/collapse (e.g., Brun and Faccenna, 2008, Yamato et al., 2008, Guillot et al., 2009, Hacker et al., 2010, Little et al., 2011, Burov et al., 2014, Chen et al., 2022). As such, UHP exhumation in the rock record is often interpreted to signify an important shift in the tectonic and geodynamic regime of an orogen (e.g., O'Brien et al. 2001; Yamato et al., 2008, Guillot et al., 2009, Hacker et al., 2010, Soret et al., 2021, Chen et al., 2022), However, the exact relationships between continental UHP exhumation and the geodynamics of orogenesis and plate tectonics, as well as the mechanisms that facilitate this process, remain poorly constrained due to the difficulty of investigating UHP metamorphism and exhumation from the bedrock record (Hacker and Gerya, 2013, Warren, 2013, O'Brien, 2019).To better understand the processes of continental UHP exhumation and its impacts on orogenesis and plate tectonics, we must combine petrology-based pressure-temperature (P-T) pathways with radioisotope geochronological constraints. This approach allows us to determine the timing and rates of UHP exhumation through P-T space and with respect to the orogeny. However, such attempts to constrain the timing and rates of UHP exhumation are always complicated by the uncertainty with which accessory phase ages are related to P-T paths (e.g. Kohn et al., 2017, O'Brien, 2019a). This

69 problem is clearly demonstrated in the UHP Tso Morari Complex of the NW Himalaya (Steck *et al.*,

70 1998; Epard and Steck, 2008; Guillot *et al.*, 2008), which forms the central study region of our

71 investigation.

72 The Tso Morari Complex is one of two UHP terranes in the NW Himalaya, the other being the Kaghan

73 Valley Complex, located ~450 km to the west of Tso Morari (Steck *et al.*, 1998; O'Brien *et al.*, 2001;

74 Parrish *et al.*, 2006; Epard and Steck, 2008; Guillot *et al.*, 2008; Buchs and Epard, 2019). Over the last

75 three decades, geochronological studies of Tso Morari have yielded a range of estimates for the timing

76 of UHP metamorphism and exhumation, spanning a period of 11 Ma (Leech et al., 2007; Donaldson *et*

77 *al.*, 2013; St-Onge *et al.*, 2013). Early interpretations were based on a limited number of spot analyses

78 of zircon (e.g. n=19, Leech et al., 2007), whereas the later publication by Donaldson et al., (2013)

79 provided a more robust record (n = 108) with a zircon age distribution ranging from 53 to 37 Ma, with

80 a peak at 47 – 43 Ma that provied a substantially narrowed estimate of peak UHP metamorphism. In

81 contrast, estimates from the Kaghan UHP eclogites are tightly constrained to ~46 Ma (Kaneko *et al.*,

82 2003; Parrish *et al.*, 2006; Zhang et al 2022). From these constraints, a diverse but poorly constrained

83 set of models have been proposed for the exhumation of Tso Morari and Kaghan Valley complexes

84 (Schwartz *et al.*, 2007; Kylander-Clark et al., 2008; Möller *et al.*, 2015; Boutelier and Cruden, 2018).

85 The spread of ages for UHP metamorphism and exhumation in Tso Morari, could, reflect differences

86 in analytical techniques and their inaccuracies, but a likely cause is also the difficulty and uncertainty

87 associated with linking geochronological data with independently constrained metamorphic petrology

88 (Foster and Parrish, 2006; Kohn et al., 2017, O'Brien, 2019a). This problem is compounded further in

89 the Tso Morari complex because UHP rocks exist as metre-scale eclogite facies mafic pods hosted

90 within amphibolite facies felsic gneiss. Accessory phases suitable for geochronology are rare in eclogite

91 pods, so some studies have attempted to relate the P-T evolution of eclogite pods with geochronological

92 constraints from the amphibolite facies gneiss (St-Onge et al., 2013). However, this approach carries

93 additional uncertainties surrounding the structural and metamorphic relationships between the eclogite

94 pods and the amphibolite facies gneiss in which they are hosted (O'Brien, 2018).

95 To overcome these problems, estimates of the timing of UHP exhumation are better resolved using a

96 combination of modern petrochronology techniques (Kohn et al., 2017), and where mineral size and

97 zonation allows, high precision techniques (Parrish et al., 2006). The former can utilise a range of

98 approaches, including: 1) the combination of geochronology, trace element geochemistry and

99 metamorphic petrology, to quantitatively relate precise ages to specific stages on a metamorphic P-T

100 path (e.g. Rubatto, 2002; Rubatto and Hermann, 2003); and 2) identifying and selecting a range of

101 accessory phases associated with different metamorphic assemblages and lithologies, which

102 collectively span a wide range of closure temperatures (Regis et al., 2016; Lotout et al., 2018; Tual et

103   al., 2022). Such techniques provide the best opportunity to accurately and precisely constrain the timing
104   of UHP exhumation.

105   In this study, we employ a range of petrochronological techniques to precisely constrain the timing of
106   UHP metamorphism and exhumation of the Tso Morari Complex. We use detailed petrographic
107   analyses, including major and trace element x-ray maps of garnet, to identify and relate prograde, peak,
108   and retrograde metamorphic assemblages in mafic eclogite samples and amphibolite facies felsic gneiss
109   samples (the Puga gneiss). This allows us to select a variety of accessory phases from different
110   metamorphic assemblages for U-Pb geochronology, to constrain the timing of metamorphism at
111   different points of the P-T path. Using laser ablation inductively coupled plasma mass spectrometry
112   (LA-ICP-MS), we analyse zircon and rutile from an eclogite pod sample, and zircon, rutile, and
113   xenotime from a felsic gneiss sample to constrain the timing of prograde, peak, and retrograde
114   metamorphism. In addition, we analysed zircon from the eclogite using chemical abrasion isotope
115   dilution thermal ion mass spectrometry (CA-ID-TIMS) to more precisely constrain the timing of zircon
116   crystallization. Our results suggest that the onset of exhumation of Indian continental crust from UHP
117   conditions occurred synchronously across the Tso Morari complex and Kaghan Valley complex at ~47-
118   46 Ma.

119   **1.2 The geodynamic significance of UHP exhumation**

120   After presenting our new geochronology data and interpreting its implications for the metamorphic
121   evolution of the Tso Morari complex, we then consider the geodynamic implications of our new
122   constraints for the Himalayan orogeny and the wider tectonic plate network. The early stages of
123   continental collision involve a shift in the geodynamics of subduction due to the positive buoyancy of
124   continental crust on the down-going plate (Afonso and Zlotnik, 2011, Hacker and Gerya, 2013, Warren,
125   2013, Capitanio et al., 2015, Laik et al., 2022). The exhumation of continental crust from UHP
126   conditions provides an important marker of this geodynamic shift, due to the association of UHP
127   exhumation with modification(s) to the subduction dynamics of a collision zone such as slab break-off,
128   a reduction in slab dip, and/or an increase in mechanical coupling between the upper and lower plates
129   (e.g., Guillot et al., 2008, Afonso and Zlotnik, 2011, Warren, 2013, Chen et al., 2022). The timing of
130   UHP exhumation is especially important, as this constraint allows scientists to interpret the structural,
131   metamorphic, and magmatic evolution of orogenesis with respect to changes in the subduction
132   dynamics of a collision zone and vice-versa, offering an invaluable opportunity to test geodynamic and

133   plate tectonic models of continental collision against bedrock constraints (e.g., Guillot et al., 2008,

134   Yamato et al., 2008, Capitanio et al., 2015, Chen et al., 2022).

135   More broadly, the timing of continental UHP exhumation can be used to better understand the impacts

136   of continental collision on tectonic plate networks. Continental collisions change the summative slab

137   pull forces within their encompassing plate network, either by reducing slab pull of the collision zone

138   during subduction of buoyant continental lithosphere or by removing slab pull from the collision zone

139   altogether via slab break off (e.g., Afonso and Zlotnik, 2011, Capitanio et al., 2015, Chen et al., 2022,

140   Laik et al., 2022). In some cases, this can trigger a plate network reorganization event, defined by a

141   short period (~10-20 Myr) of rapid and widespread modifications to the speed and direction of tectonic

142   plate motions and the topology of plate boundaries (e.g., Matthews et al., 2012, Gibbons et al., 2015,

143   Müller et al., 2016, Gürer et al., 2022). Understanding the causes and occurrences of these

144   reorganizations is important as they can drastically alter the course of Earth's paleogeographic and

145   tectonic evolution in a relatively short period of time.

146   Our understanding of plate network reorganizations is limited due to the difficulty of robustly

147   demonstrating a causative relationship between temporally overlapping, but spatially disparate tectonic

148   events and coeval changes in plate kinematics. This is particularly problematic when investigating

149   reorganizations associated with continental collision, due to the complexity of their bedrock record and

150   the uncertainties of geochronological constraints that obfuscate the duration and order of localized

151   events and their geodynamic relationships with network-wide modifications of plate kinematics. Faced

152   with this problem, constraints such as the timing of UHP exhumation, which directly correspond to

153   changes in subduction dynamics of a collision zone, can provide crucial geochronological markers for

154   constraining causative relationships between collisions and plate network reorganizations (e.g.,

155   Matthews et al., 2012, Gibbons et al., 2015).

156   A major plate network reorganization for the Indian, Eurasian, African, Australian, and Antarctic plates

157   is recognized by previous studies during the Eocene (Gibbons et al., 2015). This reorganization is

158   arguably associated with the Himalayan orogeny (Gibbons et al., 2015, Zahirovic et al., 2016), but

159   uncertainty in the collision history of the orogeny (e.g., Hu et al., 2016; van Hinsbergen et al., 2019;

160   Kapp & DeCelles, 2019; Parsons et al., 2020) means that a precise and unambiguous timestamp linking

161   the bedrock record of the orogen with the Eocene plate network reorganization has been lacking. It is

162   therefore unclear exactly how the structural and metamorphic evolution of the Himalayan orogeny

163   relates to and/or caused plate kinematic changes during the Eocene reorganization. Our new, precise

164   geochronometric constraints for the UHP exhumation in the NW Himalaya present a valuable

165   opportunity to evaluate the temporal relationships between the Himalayan orogeny and the Eocene plate

166   network reorganization and consider their causative links. With the modern advent of the user-friendly

167   GPlates plate reconstruction application (Müller et al., 2018), similar integrated analyses of collisional

168   metamorphism and plate kinematics could be used to better understand the plate tectonic consequences

169   of other orogenies.

2. Geological Background

2.1. The Himalayan orogeny and the India-Asia collision: Definitions

172   In order to interpret our data with respect to the Himalayan orogeny and India-Asia collision, it is

173   necessary to outline some definitions used hereafter. Working hypotheses for tectonic formation of the

174   Himalayan orogeny and the India-Asia collision can be broadly categorized into "Single Collision" and

175   "Double Collision" models (e.g., Hu et al., 2016; Kapp and DeCelles, 2019, Parsons et al., 2020). Single

176   Collision models propose a single continental collision between India and Eurasia, beginning at ~61

177   Ma (An et al., 2021) with convergence and under thrusting continuing to the present day (e.g., Gansser,

178   1966; Le Fort, 1975; Hu et al., 2016, Ingalls et al., 2016). Such models are not considered tenable as

179   they require extreme volumes of continental subduction and do not adequately explain the significant

180   kinematic and geodynamic changes which occur within the orogen and the surrounding plate network

181   between 50-40 Ma (e.g., van Hinsbergen et al., 2019, Parsons et al., 2020, Parsons et al., 2021). As

182   such, the results of this study are interpreted in the context of the competing "Double Collision" models,

183   for which two alternative working hypotheses exist, differing with respect to the nature of the first

184   collision. In both hypotheses, "first collision" began at ~61 Ma (e.g., Hu et al., 2015; An et al., 2021)

185   but corresponds, to either (1) collision of the Indian continent with an equatorial Neotethys intra-oceanic

186   arc (e.g., Patriat & Achache, 1984; Stampfli and Borel, 2004; Bouilhol et al., 2013; Replumaz et al

187   2014; Burg and Bouilhol, 2019); or (2) collision between an India-derived *microcontinent* and the

188   Eurasian active margin (e.g., Sinha Roy, 1976; van Hinsbergen et al., 2019; Zhou and Su, 2019).

189   "Second collision" occurred between the Indian continent and the Eurasian active margin sometime

190   between 50 Ma to 25 Ma (e.g., Patriat & Achache, 1984; Replumaz et al 2014; Burg and Bouilhol,

191   2019, Searle, 2019, van Hinsbergen et al., 2019, Parsons et al., 2021).

192   In the context of these double collision models, the Himalayan orogeny corresponds to the deformation

193   of Indian continental crustwhich initiated during first collision and continued through second collision.

194   In contrast, the "India-Asia collision" *sensu-stricto* corresponds to the second collision event only (e.g.,

195   Parsons et al., 2020; 2021). Debate continues to surround the relative validity of the two "double

196   collision" hypotheses and further considerations can be found in recent reviews (e.g., Kapp and

197   DeCelles, 2019, Searle, 2019, van Hinsbergen et al., 2019, Parsons et al., 2020); our study is presented

198   in the context of both double collision models (e.g., Burg & Bouihol 2019 versus van Hinsbergen et al.

199   2019) as it is beyond the scope of the new data presented in this paper to address their relative validity.

2.2. Geology of the Tso Morari Complex

201   The Tso Morari dome is situated on the north-western margin of the Indian plate (Fig. 1), and is
202   separated from the Ladakh batholith of the Asian plate located to the north by the Indus suture zone
203   (Fuchs and Linner, 1996). The Tso Morari dome comprises a set of stacked nappes, folded into a
204   northwest-southeast trending periclinal antiform. (Steck et al., 1998; Buchs and Epard, 2019). The
205   structurally lowermost nappe is the Tso Morari Complex (also known as the Tso Morari Gneiss, Epard
206   & Steck, 2008), which crops out in the centre of the dome. The Tso Morari Complex contains
207   Ordovician granite and disrupted mafic dykes and sills intruded into Cambrian sediments of the Indian
208   continent. Granitic rocks are variably deformed, resulting in an array of undeformed metagranites,
209   augen gneiss and garnet-mica-schists within the Tso Morari Complex. The range of deformation states
210   preserves different parts of the P-T-t history of the Tso Morari Complex. The early subduction-related
211   history is rarely preserved except as thin corona textures in low strain metagranite (Bidgood et al, 2022),
212   whereas the high strain gneisses are often overprinted by later, amphibolite facies metamorphism and
213   exhumation-related deformation. These end-member states are distinguished locally as the Polokongka
214   La granite and the Puga Gneiss, which share the same granitic protolith, and differ only in their state of
215   strain and metamorphic evolution (Girard and Bussy, 1999).

216   Mafic rocks within the Tso Morari complex locally preserve eclogite-facies mineral assemblages
217   formed at conditions of > 26 kbar, 500-645°C (e.g. de Sigoyer and Guillot, 1997; Guillot et al., 1997;
218   St-Onge et al., 2013; Bidgood et al., 2020). Evidence of high-pressure metamorphism is rarely observed
219   in the felsic metagranitoid rocks but has been recorded by glaucophane-bearing metasediments (Guillot
220   et al., 1997), pseudomorphs after coesite within the Polokongka La granite (Bidgood et al., 2020) and
221   thin corona textures (garnet, phengite, ilmenite) and pseudomorphs (kyanite, garnet and phengite) after
222   cordierite in low strain metagranites (Bidgood et al, 2022). Later overprinting at amphibolite-facies
223   conditions is recorded in the retrogressed   eclogites at 610 ± 30°C at 9 ± 3 kbar (de Sigoyer et al.,
224   1997) and in the felsic rocks at 650 ± 50°C at 9 ± 1 kbar (Girard, 2001), 630°C ± 30°C at 9 ± 2 kbar
225   (Guillot et al., 1997) and 725 ± 50°C at 7.1 ± 1.0 kbar (St-Onge et al., 2013).

226   This study describes the record of subduction-related major and accessory mineral growth preserved in
227   a rare garnet-bearing Puga Gneiss which records a part of the P-T-t history not preserved elsewhere.
228   Additionally, new data is presented which tightly constrains zircon growth in the mafic eclogites, which,
229   in conjunction with the observations in the Puga Gneiss, allows us to place the petrographic
230   observations in a geochronologic and geodynamic context.

231
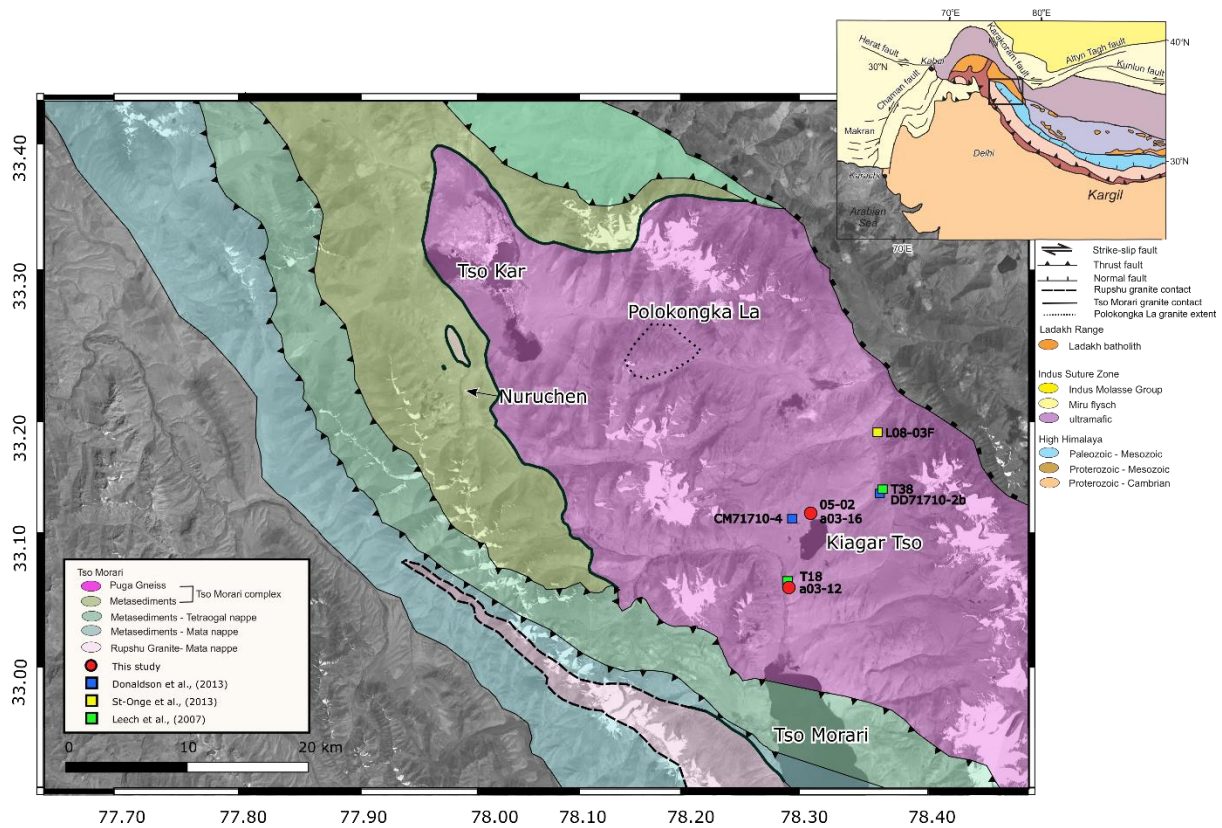
Figure 1. Geological map adapted from Epard and Steck (2008), St-Onge et al. (2013) and references therein, showing location of geochronological samples. Background USGS landsat data downloaded from *https://earthexplorer.usgs.gov/*. Colouring corresponds to bands 762, greyscale by luminosity.

2.3 Geochronology of the Tso Morari Complex

The range of estimates for UHP metamorphism and exhumation in the Tso Morari complex (54 – 44.5 Ma, Leech et al., 2007; St-Onge et al., 2013; Donaldson et al., 2013) is less tightly resolved than the age estimates for Kaghan (~46 Ma, Kaneko et al., 2003; Parrish et al., 2006; Zhang et al., 2022). Given the differences in analytical techniques used to date the Tso Morari complex and the difficulty in relating these dates to metamorphic stages, it remains unclear to what degree the spread of ages from Tso Morari can be assigned to geological heterogeneity or to analytical uncertainty and artefacts. For example, the absence of petrographic context in some studies makes it difficult to interpret the age clusters with respect to specific metamorphic conditions (see O'Brien, 2006 for further discussion). Additionally, the link between zircon growth and fluid infiltration (e.g. Chen et al., 2010; Kohn et al., 2015; Chang & Zhang, 2017; Shezovatov et al., 2021) has not been explored in the context of the published data. Importantly, given the types of data yielded from Tso Morari thus far (see following summary), it is not possible to robustly constrain whether zircon growth in the mafic eclogites was prolonged or punctuated, and whether the range of dates correspond to prograde, peak and/or retrograde metamorphic conditions. Given the narrow age range for UHP metamorphism from Kaghan only 450 km away, comparative age estimates from Tso Morari would have significant implications for the

251 processes of continental subduction and UHP exhumation; as such, this is the primary motivation for
252 this study. Here we present new and precise ages of eclogite-facies metamorphism that can be compared
253 with the ages recorded at Kaghan, along with new in situ data which, when combined with the
254 petrographic interpretation, records an additional petrographic age and stage of the evolution of the Tso
255 Morari complex that has not been previously observed.

256 The Puga Gneiss and Polokongka La granite contain zircon with thin metamorphic rims surrounding
257 igneous cores, with the latter dated by U-Pb at 479 ± 1 Ma (Girard and Bussy, 1999; Leech et al., 2007).
258 Initial estimates of the age of high pressure metamorphism by De Sigoyer et al. (2000) used Lu-Hf
259 isochron ages on garnet-clinopyroxene-whole-rock data, Sm-Nd on garnet-glaucophane-whole-rock
260 data, and U-Pb in allanite, giving ages of 45 ± 4.4 Ma, 55 ± 12.0 Ma and 55 ± 17.0 Ma, respectively.
261 These estimates attempted to date minerals which can definitively be linked to metamorphic
262 reactions/conditions, but this was hindered by the large uncertainties on these dates.

263 A spread in zircon dates from 55 to 45 Ma was recorded in the Puga Gneiss by Leech et al (2007) by
264 U-Pb SHRIMP   dating of the metamorphic rims found around igneous zircon grains (n = 19; 4 ages
265 interpreted). Sub-concordant data were split into groups arbitrarily (see O'Brien, 2006), and interpreted
266 to represent ultrahigh-pressure metamorphism at 53.3 ± 0.7 Ma, followed by further zircon growth in
267 eclogite facies conditions at 50.1 ± 0.6 Ma, amphibolite facies at 47.5 ± 0.6 Ma, and a lower temperature
268 growth at 45.2 0.7 Ma. St-Onge et al. (2013) recorded monazite and allanite U-Pb SHRIMP ages of
269 45.3 ± 1.1 Ma and 43.3 ± 1.1 Ma respectively, interpreted to represent post-eclogite facies peak
270 temperature metamorphism of 7.0 – 8.4 kbar at 705 – 755 °C, based on pseudosection modelling of the
271 observed garnet breakdown reaction. Cooling through phengite, biotite and muscovite Ar-Ar closure
272 temperatures is recorded at 48.0 ± 2.0 Ma, 31.1 ± 0.3 and 29.3 ± 0.3 Ma (De Sigoyer et al., 2000)
273 respectively, with further cooling recorded by apatite and zircon fission track data at ~23.5 – 7.5 Ma
274 (Schlup et al., 2003). Dates from within the Puga Gneiss are dominated by post-peak, amphibolite facies
275 ages recording Barrovian metamorphism, cooling and uplift.

276 The mafic eclogites better preserve the early high-pressure metamorphic history in their major and
277 accessory mineral assemblages. St-Onge et al (2013) analysed zircon in situ with SHRIMP U-Pb
278 geochronology, yielding an age of 58.0 ± 2.2 Ma (n = 2) for zircon included in the core of a garnet, and
279 50.8 ± 1 Ma (n = 4) for zircon included/adjacent to matrix barroisite, phengite and garnet. The older
280 age is interpreted to record zircon crystallisation during prograde garnet growth to high pressure, and
281 the younger age is interpreted to represent peak metamorphism in the eclogite facies. Whilst the St.
282 Onge et al. (2013) study provides a textural constraint on the prograde zircon ages which was previously
283 unknown, the data include a limited number of spots and the presence of common lead. Donaldson et
284 al. (2013) used in situ split-stream LA-ICP-MS to measure U-(Th)-Pb combined with REE
285 concentrations of zircon from two mafic eclogites, located ~10 km apart. Lower intercept dates of each

286 sample overlap at 45.3 ± 1.6 Ma and 44.2 ± 1.2 Ma. These ages broadly overlap with that of Kaghan,
287 as highlighted by Donaldson et al. (2013), but these authors also argue for protracted zircon
288 crystallisation in the eclogite facies (ca. 47 – 43 Ma) based on the spread of single spot dates and
289 consistent REE signatures with an absence of an Eu anomaly and flat HREE profiles. The Donaldson
290 et al. (2013) results improve upon the constraints of St. Onge et al. (2013) based on the number of data,
291 but are still hampered by both the presence of common lead and the precision of the in situ method
292 which yields single spot uncertainties of ca. 1 to 10 Ma.

293 The age of UHP metamorphism in the Kaghan Valley Complex has been estimated using U-Pb
294 SHRIMP and U-Pb ID-TIMS analyses of zircon from eclogite-facies mafic rocks, yielding ages of 46.2
295 ± 0.7 Ma (Kaneko et al., 2003) and 46.4 ± 0.1 Ma (Parrish et al., 2006), respectively. These zircons
296 were found included in UHP garnet rims with coesite inclusions. Eclogite facies ages of zircon and
297 allanite from Kaghan were also estimated using U-Pb and Th-Pb ID-TIMS analyses at 45.5 ± 6.6 Ma
298 and 46.5 ± 1.0 Ma, respectively (Parrish et al., 2006). An additional age of eclogite facies zircon was
299 estimated using U-Pb SIMS at 46 ± 2 Ma in Naran, 30 km south-west of Kaghan (Zhang et al., 2022).
300 A compilation of geochronology of high pressure metamorphism in the north west Himalaya can be
301 found in Supporting Information 1 and is compared to our new data in Figure 8.

3. Petrography

3.1. Analytical methods

304 Petrographic study of 29 mafic eclogites and 28 Puga Gneiss samples from the Tso Morari Complex
305 was undertaken, with one fresh eclogite (a03-16), one retrogressed eclogite (a03-12) and one gneiss
306 sample (05-02) selected for further petrological analyses. Major element compositions of minerals that
307 exhibit solid solutions were measured using a Cameca SX-5 field emission electron microprobe at the
308 University of Oxford, with a 15 kV acceleration potential, 20 nA beam current, 30 second count time
309 per major element (30 second background) and 60 second count time on Ti (60 second background). A
310 range of natural and synthetic oxide standards were used including albite (Na, Al, Si), Orthoclase (K),
311 MgO (Mg), wollastonite (Ca), andradite (Fe), Mn metal (Mn) and synthetic TiO_2 (Ti) and analyses
312 were verified against secondary mineral standards. Mineral spot analyses and line profiles were taken
313 across garnet to determine the extent of intracrystalline compositional variation (see Supporting
314 Information 2).

315 Quantitative major element X-ray maps of garnets were collected from polished thin sections using the
316 CAMECA SX-5 field emission electron microprobe at the University of Oxford at a working distance
317 of 10 mm, a 15 k   V acceleration potential, 170 nA current, 0.06 s dwell time and a 3 µm step size for
318 the elements P, Ca, Mn, Mg and Fe. A dwell time of 0.032 s and a 200 nA beam current were used for

319   the elements Al, Si, Ti, Y and Yb. A range of natural and synthetic oxide standards were used including

320   Durango apatite (P), andradite (Ca, Fe), Mn metal (Mn), MgO (Mg), albite (Al, Si), TiO2 (Ti), Y metal

321   (Y), Yb metal (Yb).

322   **3.2. Petrography and petrology: Observations**

323   *3.2.1. Puga Gneiss (sample 05-02)*

324   Puga Gneiss sample 05-02 was collected from the north shore of Kiagar Tso (33.1214°N, 78.2958°E),

325   in the middle of the Tso Morari Complex. Sample 05-02 is a strongly-foliated, garnet-bearing gneiss

326   comprising albite, quartz, muscovite, biotite and garnet, with accessory zircon, apatite, rutile, and

327   xenotime. Sample 05-02 shows a schistosity (S2) defined by bands of white mica, albite and quartz

328   (Fig. 2a) which wrap around larger garnet porphyroblasts. Quartz occurs in polycrystalline ribbons or

329   lenses separated by narrow bands of white mica, indicative of a high-strain fabric (Fig. 2a-d). The quartz

330   ribbons are cut by discontinuous shear bands forming an S-C′ fabric. Quartz grains are > 200 µm and

331   equant with amoeboid shapes along grain boundaries indicative of grain boundary migration (GBM)

332   dynamic recrystallisation (e.g. Stipp et al., 2002). Albite bands and lenses are largely composed of fine-

333   grained aggregates. Among these, larger feldspar grains show subgrains of similar size to the dominant

334   population, suggesting that dynamic recrystallization occurred in the subgrain rotation (SGR) regime

335   for feldspar (Passchier & Trouw, 2005). Zircon and rutile occur in the matrix.

336

337   Garnet porphyroblasts of varying size are scattered through the rock. They are abundantly fractured,

338   and partly replaced by biotite, white mica and chlorite. The studied section contains one large (6 x 5

339   mm) ovoid garnet porphyroblast (Fig. 3) that contains significant textural complexity (see below). Fine-

340   grained inclusion trails of quartz and rutile define a primary foliation (S1), which is oblique to the

341   matrix fabric (S2) and folded at the core-rim boundary (Fig. 3a). Kyanite occurs within the garnet core,

342   adjacent to staurolite, surrounded by white mica (Fig. 3a). The garnet is subhedral with   embayments

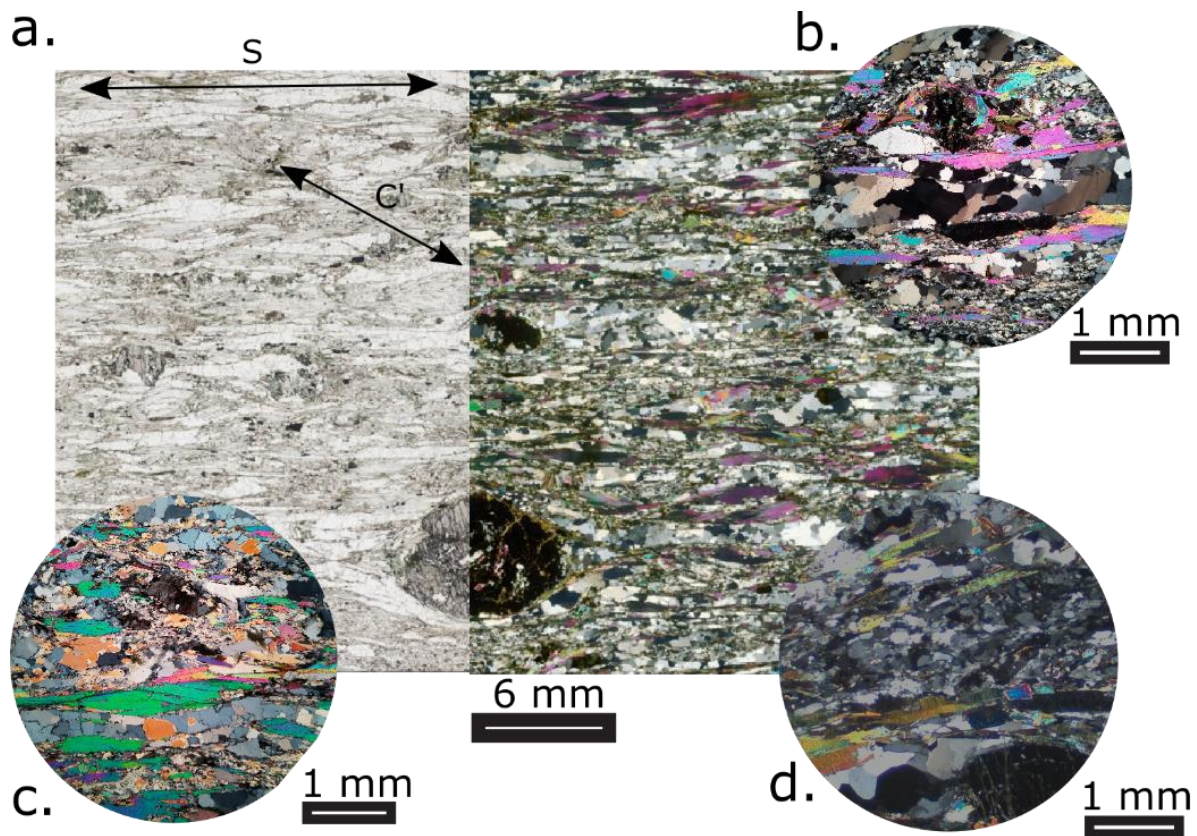343   containing biotite, white mica and xenotime (Fig. 3a).

344

Figure 2. a. Puga Gneiss Sample 05-02. PPL and XPL image showing gneissose texture consisting of quartz-rich, feldspar-rich and mica-rich layers. Large garnet wrapped by fabric (S2) shown in Figure 3. b-c Puga Gneiss Sample 05-01, adjacent to 05-02. b. Polycrystalline quartz-rich band in between mica sheets. Recrystallised quartz shows undulose extinction. Quartz grains in the lower part of the image span the width of the mica ribbons. c. Stacked white mica sheets curve into high strain fabric showing top to the right sense of shear. Annealed quartz band and dusty albite and apatite present. d. Puga Gneiss Sample 05-02. Fine-grained albite lens between mica sheets.
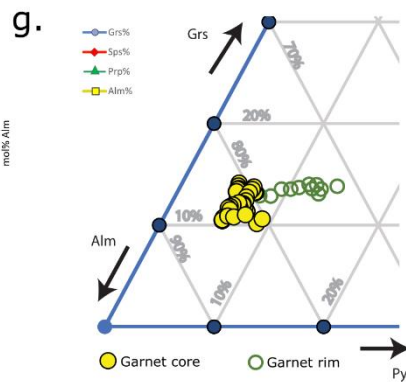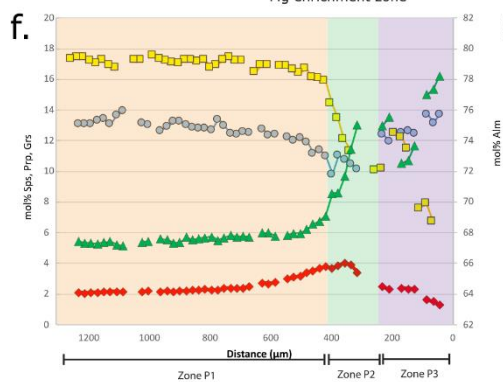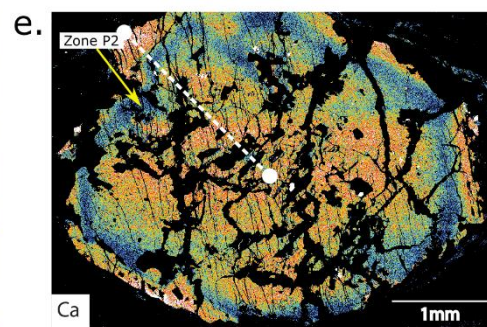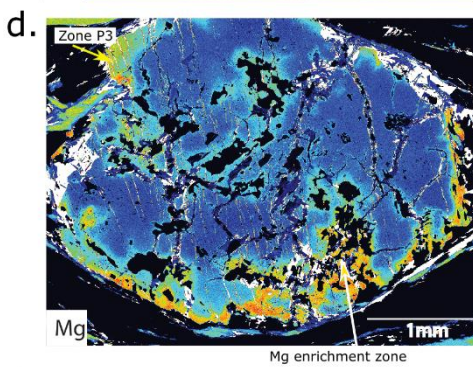
a.

Y annulus

truncation

Xenotime
Fe oxide
Apatite
Kyanite
Rutile
Rutile inclusion trail

1mm

b.

Y annulus

Zone P2

Y

1mm

c.

Zone P1

Mn

1mm

d.

Zone P3

Mg

Mg enrichment zone

1mm

e.

Zone P2

Ca

1mm

f.

Grs%
Sps%
Prp%
Alm%

Zone P1   Zone P2   Zone P3

mol% Sps, Prp, Grs

mol% Alm

Distance (µm)

g.

Grs%
Sps%
Prp%
Alm%

Grs

Alm
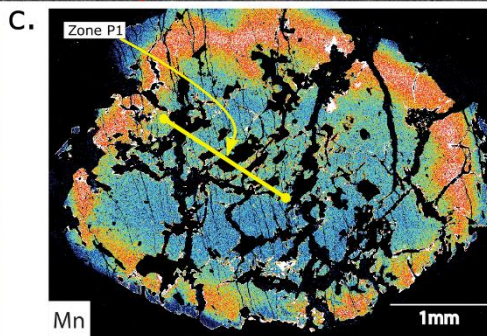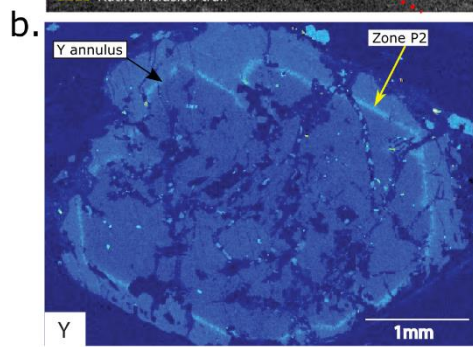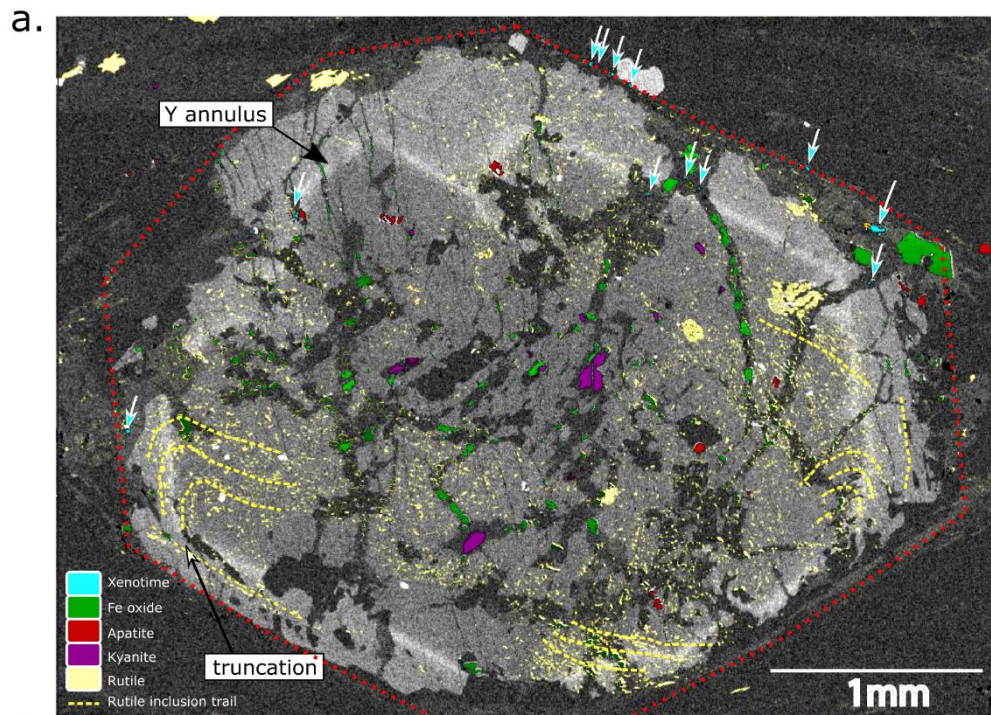
Py

Garnet core   Garnet rim

352

353 Figure 3. Puga Gneiss Sample 05-02 garnet. a. The brightest grains from the Ti map (yellow), Ca map
354 (red), Fe map (green), Y map (cyan) and Al map (purple) are overlain on an Y map adjusted for Y-
355 zonation in garnet. The location of xenotime grains can be identified based on the brightest Y locations
356 to correspond with the micaceous rim after garnet. The map also highlights the orientation of rutile
357 inclusion trails and the location of rectangular rutile clusters. The approximate outline of the original
358 garnet is highlighted as a red dashed line. b-e. Yttrium, manganese, magnesium and calcium EPMA
359 element maps. Location of the core-rim boundary defined by the yttrium high. f . Garnet zoning profiles
360 from core (left) to rim (right). g. Ternary diagram of transect across garnets. Approximate location of
361 garnet transect shown by white dashed line on panel e.

362

363 Garnet exhibits concentric zonation, comprising three distinct zones (Fig. 3). The garnet core (zone P1,
364 Fig. 3c) has an approximately uniform composition of $Alm_{79.0}Grs_{12.5}Pyr_{5.5}Spss_{4.0-2.3}$. Inclusions of
365 quartz, rutile and white mica are found throughout zone 1, whereas inclusions of kyanite are restricted
366 to the inner portion of zone P1 (Fig. 3a,f). Zone P2 (Fig. 3b,d,f) is marked by a decrease in Ca and
367 increase in Mn. It contains a narrow annulus of high Y content, and its outer boundary is faceted. The
368 narrow rim zone P3 (Fig. 3d,f) shows a marked increase in Mg (to 16% pyrope) and Ca (to 13%
369 grossular), with lower Mn. It is discontinuous around the garnet margin. Zones P2 and P3 contain
370 quartz, white mica, and rutile inclusions, but to a lesser extent than in zone 1. Kyanite is absent from
371 zones P2 and P3. In zones P1 and P2, magnesium-enriched haloes are developed along the internal
372 fracture network, surrounding many larger inclusions of white mica and quartz, and connecting with
373 the outer zone of the garnet.

374

375 *3.2.2. Mafic eclogite (sample a03-16)*

376

377 Sample a03-16 is a mafic eclogite taken from the same locality as Puga Gneiss sample 05-02
378 (33.1214°N, 78.2958°E), adjacent to sample CM71710-4 of Donaldson et al. (2013), and displays
379 similar features to mafic eclogites described from other localities in the Tso Morari Complex (e.g.
380 Jonnalagadda et al., 2017; O'Brien & Sachan, 2000; Palin et al., 2014; St-Onge et al., 2013; Wilke et
381 al., 2015). Sample a03-16 has a medium- to coarse-grained granoblastic texture with a major mineral
382 assemblage of garnet, omphacite, phengite, quartz, and talc, with minor amounts of clinozoisite,
383 amphibole, carbonate, rutile and zircon.

384

385 Garnet and omphacite (Fig. 4a) are in textural equilibrium, forming planar contacts, with coarse grained
386 homogeneous phengite and talc. In some places, symplectites after omphacite are observed, comprised

387   of amphibole, plagioclase and occasional diopside. Dolomite is also present in the matrix as large

388   poikiloblasts containing inclusions of phengite, omphacite and rutile.

389

390   Amphibole occurs in the matrix and as inclusions in garnet (Fig. 4b). In common with other sampled

391   outcrops, coarse-grained matrix amphibole typically has pale green winchite cores, zoned towards a

392   pargasitic composition at rims. Thin mantles of green pargasitic amphibole surround garnet, and

393   amphibole inclusions in garnet are darker blue-green pargasite and ferropargasite. Fine-grained

394   intergrowths of biotite and plagioclase surround phengite. Matrix quartz and omphacite contain clusters

395   of zircon inclusions, whereas garnet, omphacite, quartz, phengite, and talc contain rutile inclusions (Fig.

396   4c). Garnet occurs as subhedral porphyroblasts that are 3-4 mm in diameter (Fig. 4b) and contain

397   inclusions of zoned blue-green amphibole, and also quartz and rutile. Rutile commonly forms angular

398   clusters of grains, both in the matrix and within garnets, which we interpret as replacing a former
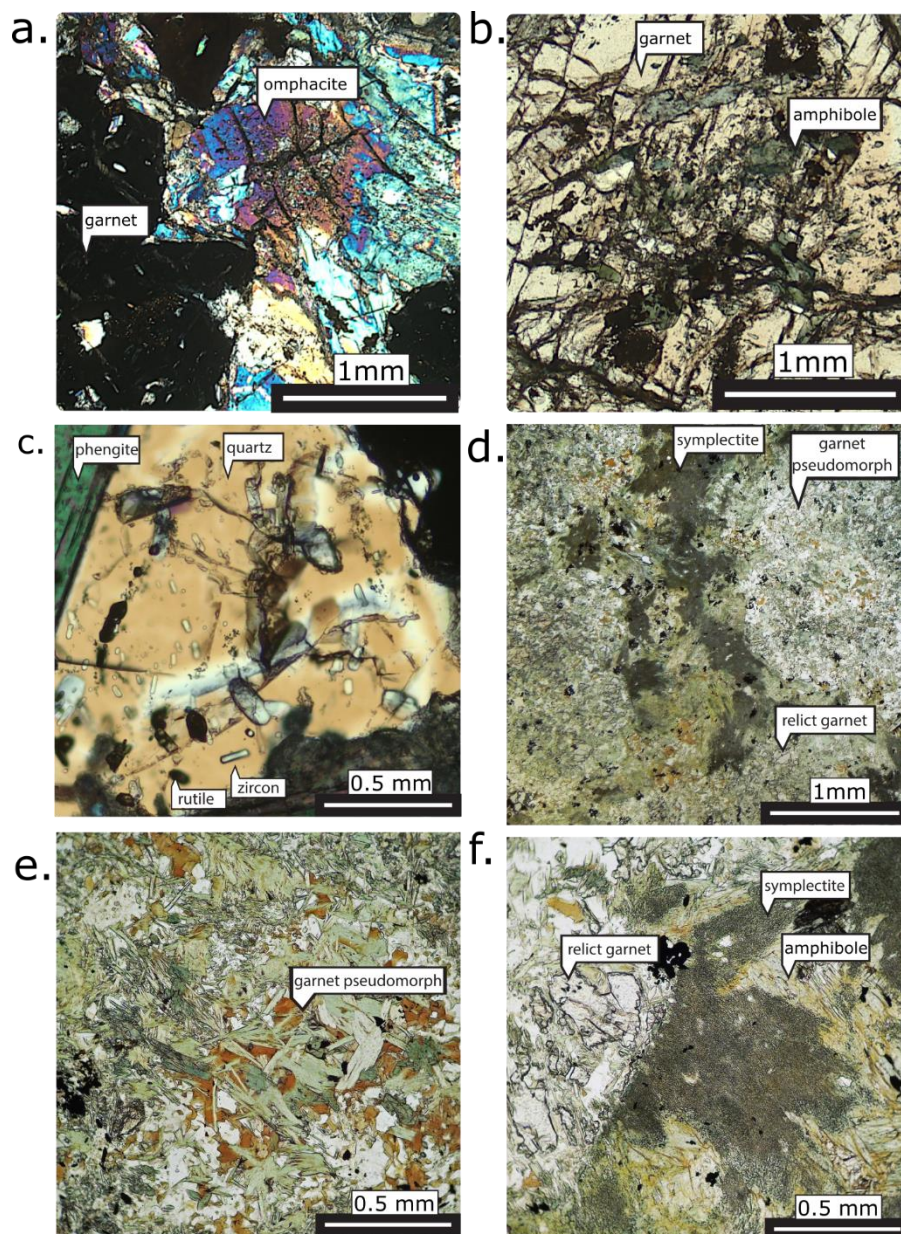
399   igneous Fe-Ti oxide.

400

Figure 4. Photomicrographs of mafic eclogites. a. Sample a03-16, XPL, poikiloblastic garnets and omphacite. b. Sample a03-16, colour zoning in garnet with amphibole inclusions ranging in colour from blue to green. c. Sample a03-16, matrix quartz with abundant high relief zircon and dark rutile inclusions. d-f. Sample a03-12 retrogressed mafic eclogite. d. Subhedral pseudomorphed garnets present on the edge of the image. Dark-coloured, fine-grained intergrowth of plagioclase and amphibole (symplectite) after omphacite. Coarse-grained, green matrix amphiboles interlocked with omphacite pseudomorphs. e. Core of large pseudomorphed garnet showing aggregate of chlorite, biotite and minor green amphibole set in plagioclase. f. Dark amphibole-plagioclase symplectite after omphacite adjacent to partly pseudomorphed garnet.

410

411 Major and trace element maps of a single garnet in sample a03-16 show three zones (Fig. 5). Zone E1

412 (Fig. 5d) defines the core region, which has a composition of Alm48-42 Grs24-29 Pyr20-30 Sps6-1,

413 with increasing almandine and pyrope components from core to rim (Fig. 5 b and c). The rim of the

414 zone E1 core is outlined by a   Mn-rich annulus. Zone E2 surrounds the zone E1 core and is defined

415 by a calcium trough with a faceted outline (Fig. 5 d and e). Zone E3 (Fig. 5b) forms along the garnet

416 rim defined by a Mg-rich, Mn-poor rim with shows an increase in pyrope (to 30-35%) and grossular

417 (to 30%, decreasing to 16% at the outer rim).   Mg-   rich E3-like domains also extend in some places

418 from the outer rim towards the core of the garnet, cutting across concentric garnet zones E1 and E2, and

419 surrounding inclusions, often forming channelized features (Fig. 5 b and c).
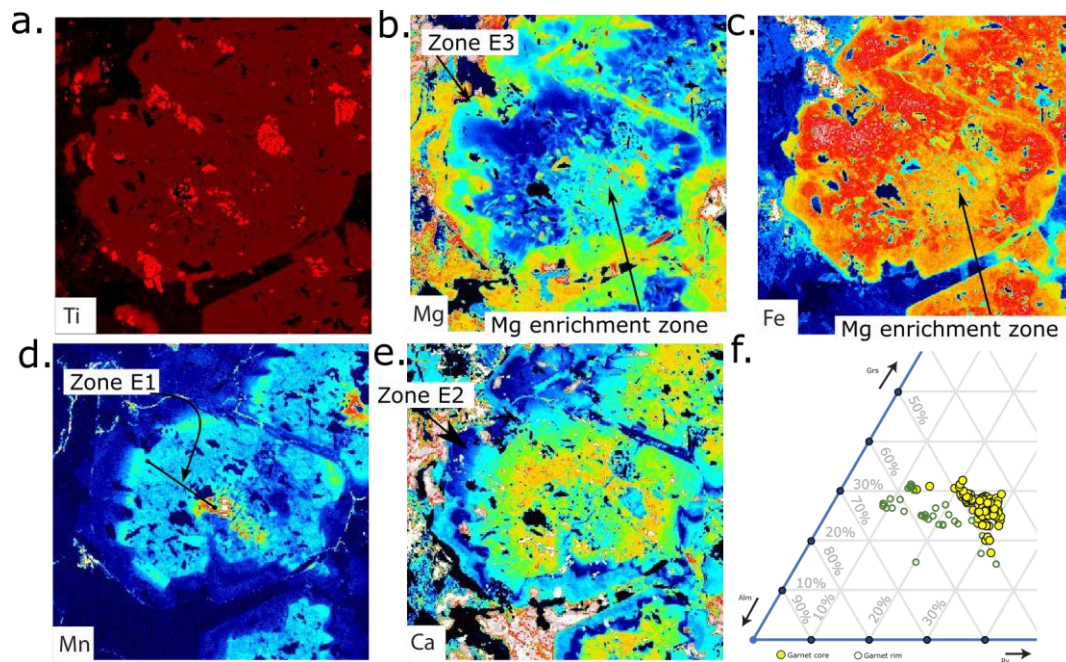

420

421 Figure 5. Garnet maps from mafic eclogite sample a03-16. a. Ti map showing clusters of rutile

422 inclusions forming distinct shapes after Fe-Ti oxides. b-e. Mg, Fe, Mn and Ca maps showing concentric

423 zoning patterns cut by Mg-Fe embayments emanating from the outside rim of the garnet. f. Ternary

424 diagram of transect across garnet showing Fe-Mg alteration and garnet rim.

425

426 **3.2.3. Retrogressed mafic eclogite (sample a03-12)**

427

428 Sample a03-12, along with the adjacent sample a03-09, is a retrogressed mafic eclogite from 'The

429 Bridge' locality (33.0677°N, 78.2758°E), ~8 km south of sample a03-16. This is the same locality

430 sampled and analysed by Leech et al. (2007) (their sample T18). The sample is composed of garnet,

431 amphibole, plagioclase, biotite, chlorite, ilmenite, rutile and zircon. Relict garnet is preserved within

432 pseudomorphs that preserve subhedral garnet shapes, but are largely replaced by plagioclase,

433 hornblende, biotite and chlorite aggregates (Fig. 4 d and e). Former matrix omphacite has been

434   overprinted by coarse-grained blue-green sodic-calcic amphibole (cf. Palin et al., 2014), and

435   subsequently pseudomorphed by fine-grained amphibole-plagioclase intergrowths (Fig. 4f).

436   Chlorite and biotite form aggregates which overprint the surrounding metamorphic patterns. Rutile

437   grains occur in garnet and matrix amphibole, and are rimmed or replaced by ilmenite in retrogressed

438   areas. Zircon   occurs as small grains in the matrix.

439

440   **3.3. Petrography and petrology: Interpretation and metamorphic correlation**

441   *3.3.1. Puga Gneiss (sample 05-02)*

442   The Puga Gneiss (sample 05-02) displays evidence of two metamorphic assemblages. The first is

443   defined by the garnet compositional zoning, and the inclusion suite of quartz, kyanite, rutile and zircon.

444   Quartz and rutile inclusions define a crenulated primary foliation (S1). Kyanite is found exclusively

445   within garnet. The garnet compositional zoning has features that match the zoning in eclogite garnet

446   (cf. St-Onge et al, 2013, and Fig. 5), i.e. a Ca-rich core (P1 = E1), Ca-poor trough (P2 = E2) and Mg-

447   and Ca-rich rim (P3 = E3). This is consistent with prograde growth culminating in eclogite-facies

448   conditions (e.g. St-Onge et al., 2013; Wilke et al., 2015; O'Brien, 2019b). The Mg distribution in the

449   garnet interior implies that some fracturing occurred at near-peak conditions.

450

451   The second assemblage is defined by the rock matrix grains outside the garnet porphyroblasts, which

452   form a segregated quartz-feldspar-mica mineral banding modified by an S-C′ fabric. Accessory

453   minerals in this matrix assemblage include rutile and zircon. Dynamic recrystallization of quartz by

454   grain boundary migration suggests a deformation temperature in excess of 530°C (Stipp et al., 2002),

455   and evidence for subgrain rotation in albite is consistent with about 600°C (Passchier & Trouw, 2005).

456   No lower-temperature dynamic recrystallization microstructures are observed, and minor chlorite,

457   generally associated with garnet, is undeformed. Rutile is stable in the rock matrix, commonly enclosed

458   in white mica. Based on these observations, we interpret the matrix assemblage to reflect metamorphism

459   and deformation on the retrograde path, at amphibolite-facies conditions.

460

461   A distinct mineral association surrounds the large garnet in sample 05-02, where parts of the Mg-rich

462   rim zone (P3) of the garnet are missing, due to partial resorption of garnet, and micaceous aggregates

463   in embayments and fractures host xenotime grains (Figure 3a).

464

465   *3.3.2. Mafic eclogite (sample a03-16)*

466   Sample a03-16 contains three identifiable metamorphic assemblages. Garnet and omphacite (Fig. 4a)

467   in textural equilibrium with coarse grained homogeneous phengite and talc define a peak pressure

468   eclogite-facies mineral assemblage (e.g., M2 of St-Onge et al., 2013). Accessory phases within this
469   peak assemblage include zircon, present as clusters of grains included within matrix quartz and
470   omphacite, and rutile, present as inclusions, commonly clustered, within garnet, omphacite, quartz,
471   phengite, and talc (Fig. 4c). Inclusions of zircon and rutile in garnet cores suggest that   initial growth
472   of these grains may have begun prior to eclogite facies metamorphism. Within garnet, the increase in
473   pyrope component from core to rim, corresponds to garnet growth during prograde to peak eclogite
474   conditions. We interpret zones E1 to E3 as a prograde to peak assemblage, where zone E3 correlates
475   with the omphacite, phengite and talc peak assemblage described above. The second metamorphic
476   assemblage is defined by the early breakdown products of the peak assemblage phases. The dominant
477   example is the zoned blue-green matrix amphibole, which may represent the product of talc dehydration
478   as well as the influx of external fluids under eclogite-facies conditions (cf. Palin et al., 2014). The third
479   assemblage includes feldspar-bearing symplectites after omphacite, and secondary fine-grained white
480   mica aggregates forming in the irregular rims of coarse-grained phengite. These represent an
481   amphibolite-facies overprint consistent with the matrix assemblage of Puga gneiss sample 05-02.
482
483   *3.3.3. Retrogressed mafic eclogite (sample a03-12)*
484   Sample a03-12 is dominated by a post-peak metamorphic assemblage, whereas the peak assemblage
485   displayed by sample a03-16, is identifiable in a03-12 as relict garnet grains and pseudomorphs after
486   garnet and omphacite. Blue-green amphiboles are interpreted as an early post-peak phase, which grew
487   within the eclogite facies field prior to the appearance of stable sodic feldspar during decompression
488   (e.g., Palin et al., 2014). The rest of the post-peak assemblage is typical of an amphibolite facies
489   retrograde assemblage characterised by fine-grained amphibole and plagioclase intergrowths.
490   Aggregates of chlorite and biotite characterise a lower amphibolite facies overprint. Rutile is found
491   within prograde relict garnets as well as the matrix and has no indication of internal zonation. We
492   therefore interpret rutile as a relict grains from a prograde or peak assemblage, rather than a new phase
493   that nucleated during latest-stage lower amphibolite facies metamorphism. Zircon is present throughout
494   this sample, predominantly as inclusions in peak omphacite and quartz, suggesting that it crystallised
495   at eclogite-facies conditions.
496
497   *3.3.4. Correlation of metamorphic assemblages (M1, M2, M3) in the Puga Gneiss and mafic eclogites*
498
499   Comparison and correlation of the petrography and petrology of samples 05-02, a03-16, and a03-12,
500   allows for the definition of three distinct metamorphic assemblages that reflect distinct portions of the
501   same P-T path of the Tso Morari complex, experienced and recorded by both lithologies. These
502   assemblages are correlated with the stages defined by St-Onge et al (2013) (M1, M2, M3). Crucially,
503   these assemblages provide a robust means for linking accessory phase geochronology to metamorphic

504 evolution of the Tso Morari complex. These metamorphic assemblages and their constituent accessory
505 phases are summarised as follows:
506

507 *3.3.4.1. M1: Prograde-to-peak eclogite facies assemblage*
508 Zones P1 and P2 of garnet within the Puga gneiss sample 05-02 and zone E1 and E2 of garnet in the
509 mafic eclogite a03-16 define the M1 prograde-to-peak, eclogite facies assemblage. This includes
510 inclusions of kyanite, quartz, white mica, zircon and rutile, within garnet in Puga Gneiss sample 05-02.
511

512 *3.3.4.2. M2: Peak eclogite facies assemblage*
513 High-Mg rims of garnet (zones P3 and E3), plus omphacite, phengite, quartz and talc in mafic eclogite
514 sample a03-16 define the M2 peak eclogite facies assemblage. M2 also includes the high-Mg garnet
515 rims in Puga gneiss sample 05-02. Elsewhere in Tso Morari, similar garnet rim compositions in mafic
516 eclogites contain inclusions of coesite or polycrystalline inclusions after coesite (Sachan et al., 2004;
517 Bidgood et al., 2021). Remnants of this assemblage are also preserved by relict garnet in the retrogressed
518 mafic eclogite sample a03-12.
519

520 *3.3.4.3. M3a/M3b/M3c: Post-peak assemblage*
521 The M3 post-peak assemblage reflects continuing metamorphism from eclogite to lower amphibolite
522 facies conditions, and is subdivided to reflect this. In the mafic eclogite samples (a03-16, a03-12), M3a
523 is recorded by growth of coarse-grained blue-green amphiboles in the eclogite facies, which elsewhere
524 in the Tso Morari Complex, has been linked to the breakdown of talc and the influx of fluid at 23 kbar
525 and 19 kbar respectively (Palin et al., 2014). Post-peak assemblage M3b corresponds to upper
526 amphibolite facies retrograde metamorphism. In the mafic eclogite samples (a03-16, a03-12) M3b is
527 defined by symplectites of fine-grained amphibole and plagioclase intergrowths after omphacite. The
528 lower-temperature association of chlorite with biotite, largely as a replacement of garnet cores in a03-
529 12, is assigned to M3c.
530

531 In Puga gneiss sample 05-02, initial garnet breakdown and the associated nucleation of xenotime,
532 occurred at eclogite to upper amphibolite facies, and therefore correlates with either the M3a or M3b
533 post-peak assemblages observed in the mafic eclogites. M3b is defined by the matrix assemblage of
534 quartz + albite + muscovite, which also contains zircon and rutile, and displays quartz microstructures
535 indicating post-peak deformation temperatures of >530 °C. M3c corresponds to lower amphibolite
536 facies retrograde metamorphism and is represented by overprinting aggregates of chlorite and biotite
537 after garnet.
538

4. U-Pb Geochronology

4.1. Analytical methods

Zircon grains from the heavy, non-magnetic fraction of sample a03-12 were imaged via cathodoluminescence (CL) using an FEI Quanta 650 environmental scanning electron microscope (E-SEM) at the University of Oxford, using a 10 kV electron beam, 16mm working distance and a beam current of 0.49nA. Zircon grains from sample 05-02 were also mounted on sticky tape in order to analyse the <10 µm thick rims. Rutile grains chosen for analysis were picked from the non-magnetic fraction and were imaged via backscatter electron imaging (using the same E-SEM) to determine the homogeneity of the grains chosen for analysis. None of the rutile grains showed any evidence of zoning. Xenotime was measured in a polished thin section in order to preserve the petrographic relationships observed.

All geochronology and mineral separation were conducted at the Geochronology and Tracers Facility, British Geological Survey, Nottingham, UK. Laser ablation inductively-coupled plasma mass spectrometry (LA-ICP-MS) was conducted using a Nu Instruments AttoM sector-field single-collector ICP-MS, coupled to an Elemental Scientific Lasers 193nm UC Excimer laser ablation system fitted with a TV2 cell. The method follows that described in Roberts et al. (2016), with uncertainty propagation following recommendations of Horstwood et al. (2016), and age calculation and plotting using IsoplotR (Vermeesch, 2018). Common lead corrected ages, where quoted, use a [207]Pb-based method (Chew et al., 2014) and assume a Stacey and Kramers (1975) initial lead composition, and concordance of the final age. All uncertainties are quoted and plotted at 2σ. LA-ICP-MS dates are quoted with propagation of systematic uncertainties, including reference material and decay constant uncertainties; age uncertainties are also expanded to account for the MSWD where the data exhibit overdispersion (Vermeesch, 2018). Accuracy based on zircon and rutile validation materials was better than 1% for zircon and xenotime and 5% for rutile (Plešovice = 339.1 ± 1.9 Ma; GJ-1 = 596.8 ± 2.9 Ma; Manangotry = 555.48 ± 4.23; R19 = 465.9 ± 3.9 Na; Sugluk = 1714 ± 30 Ma; and PCA = 1859 ± 25 Ma). Trace elements were measured using the same instrumentation as for U-Th-Pb, with the Attom measuring in linkscan mode (see Supporting Information 3 for full analytical protocol), with normalisation to GJ-1 zircon (Piazolo et al., 2017) except Ti which used Szymanowski et al. (2017).

Zircon in one sample (a03-12) was further analysed by CA-ID-TIMS, following analytical and data reduction methods described by Tapster et al. (2016), and utilising the ET535 EARTHTIME mixed tracer (Condon et al., 2015). The CA-ID-TIMS uncertainties are quoted as analytical only/analytical+tracer-calibration/analytical+tracer-calibration+decay-constant uncertainty, as per community protocols. Our U-Pb dates can be compared using the intermediate uncertainty, but for the sake of simplicity, we quote the final uncertainty within the discussion such that our dates can be compared with constraints from other absolute and relative chronometry.

576

4.2. Puga Gneiss (sample 05-02)

4.2.1. Zircon

Zircon grains in the Puga gneiss sample 05-02 show oscillatory zoning and a euhedral shape, indicative of igneous zircon, with a Th/U of 0.05 – 0.26. Thin, bright rims (< 20 μm) are present surrounding the dark cores. From the epoxy mounted zircon, 33 LA-ICP-MS analyses of zircon cores were obtained from 21 grains. Five ages ranging from 2481 Ma to 1020 Ma (^{207}Pb/^{206}Pb age), indicate a population of xenocrystic zircon inherited during emplacement of the Puga gneiss igneous protolith. Nine analyses had ages that were discordant by >10 %, and were discarded from age calculation. Of the remaining 19 concordant analyses, 17 spots provide a concordia age of 482 ± 5.9 Ma with a mean square of weighted deviates (MSWD) value of 1.5 (Fig. 6a). Using spot analysis of tape-mounted zircon, whereby the outer rim can be targeted more confidently, 64 grains yielded a spread of ages from ca. 569 Ma to 48 Ma (Fig. 6b). A broad plateau of ages overlaps the mounted zircon at ca. 480 Ma, consistent with our weighted mean concordia age. The youngest three analyses provide a weighted mean, using common lead corrected ^{206}Pb/^{238}U ages, of 48.9 ± 1.2 Ma (MSWD = 1.3; Fig. 6b).
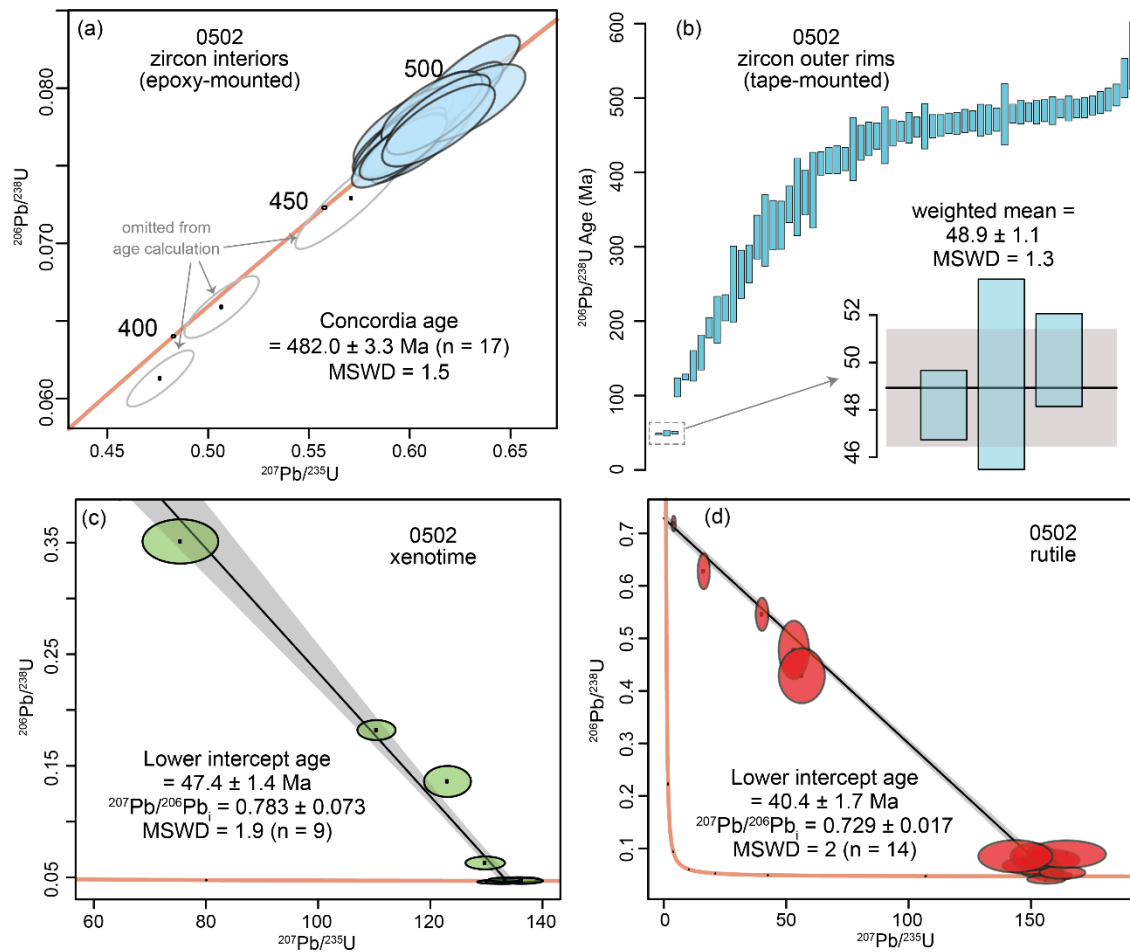

Fig. 6. A. U-Pb Wetherill plot showing U-Pb zircon core analyses of Puga Gneiss sample 05-02. B. Rank-plot of all ^{206}Pb/^{238}U zircon date   s. An older age plateau represents the zircon cores at ~480 Ma. The youngest dates represent thin rims, and converge on a Himalayan age with a weighted average

595 ^{206}Pb/^{238}U age of the three youngest zircon dates. C. Tera-Wasserburg plot of xenotime U-Pb analyses.

596 D. Tera-Wasserburg plot of rutile U-Pb analyses. Box heights and uncertainty ellipses are 2σ

597 uncertainties.

598

599 *4.2.2. Xenotime*

600 Rare 30-100 µm xenotime grains were observed in micaceous aggregates at corroded margins of garnet

601 in sample 05-02, as described above (Fig. 3a). The grains show homogenous brightness in BSE

602 indicating the absence of internal zonation. Nine spots were analysed across 9 grains, and yield a mixing

603 line between radiogenic and common lead components. Using a free regression, the lower intercept age

604 is calculated at 47.4 ± 1.4 Ma (MSWD = 1.9; Fig. 6c).

605

606 *4.2.3. Rutile*

607 Rutile grains in sample 05-02 measure 50-100 µm in size and show homogenous brightness in BSE,

608 indicating the absence of internal zonation. Fourteen spots were analysed across 14 rutile grains, and

609 yield a mixing line between radiogenic and common lead components. Using a free regression yields a

610 lower intercept age of 40.4 ± 1.7 Ma (MSWD = 2; Fig. 6d).

611

612 **4.3. Retrogressed mafic eclogite (sample a03-12)**

613 *4.3.1. Zircon*

614 Zircon grains are rarely found in mafic eclogites of the Tso Morari Complex. In thin section, zircons

615 are often found as inclusions within eclogite-facies phases such as quartz and omphacite. Separated

616 zircon grains from sample a03-12 are translucent and colourless with rounded and euhedral grain shapes

617 and a grain size of < 70 µm (Fig. 7f). They have zoning patterns dominated by broad oscillatory or

618 sector zoning, that in some grains, truncates a darker core region; the latter were not analysed.

619

620 Thirteen laser spot analyses were performed on the cores of 13 zircon grains separated from sample

621 a03-12 for U-Pb, with 3 analyses rejected due to Pb counts below detection. The U concentrations are

622 variable (13.5 – 1528 ppm), and the degree of discordance varies between 0.1 and 12%. Of the

623 remaining 10 analyses, the lower intercept of 9 spots is calculated using a free regression at 47.5 ± 1.7

624 Ma (MSWD = 0.63; Fig. 7a). These zircon analyses have low Th/U ratios (<0.01). The result implies

625 that the data conform to a single population. The omitted analysis has a much higher Th/U ratio (0.25),

626 suggesting an igneous core region was clipped during the ablation.

627

628 Trace elements were measured on 20 zircon grains, including adjacent spots on the same 13 grains

629 analysed for U-Pb; 3 analyses were omitted due to inclusions. Ti-in-zircon temperatures are calculated

630 using Si and Ti activities of 1.0, and the equation of Ferry and Watson (2007). The temperatures range

631   from 603 °C to 724 °C, forming a normal distribution around a peak at ca. 630 °C (Fig. 7c). The REE

632   data are plotted as chondrite-normalised values (Fig. 7d). The REE patterns of zircon are broadly

633   consistent across multiple grains, with no Eu anomaly, flat HREE patterns and depleted LREEs.

634

635   Several zircon grains were extracted from the resin mounts and prepared as single grain aliquots for

636   CA-ID-TIMS. The resulting data are six reproducible fractions yielding a weighted mean (Th-

637   corrected) $^{206}Pb/^{238}U$ age of 46.912 ± 0.068 Ma with an MSWD of 0.2 (Fig. 7b).

638

639
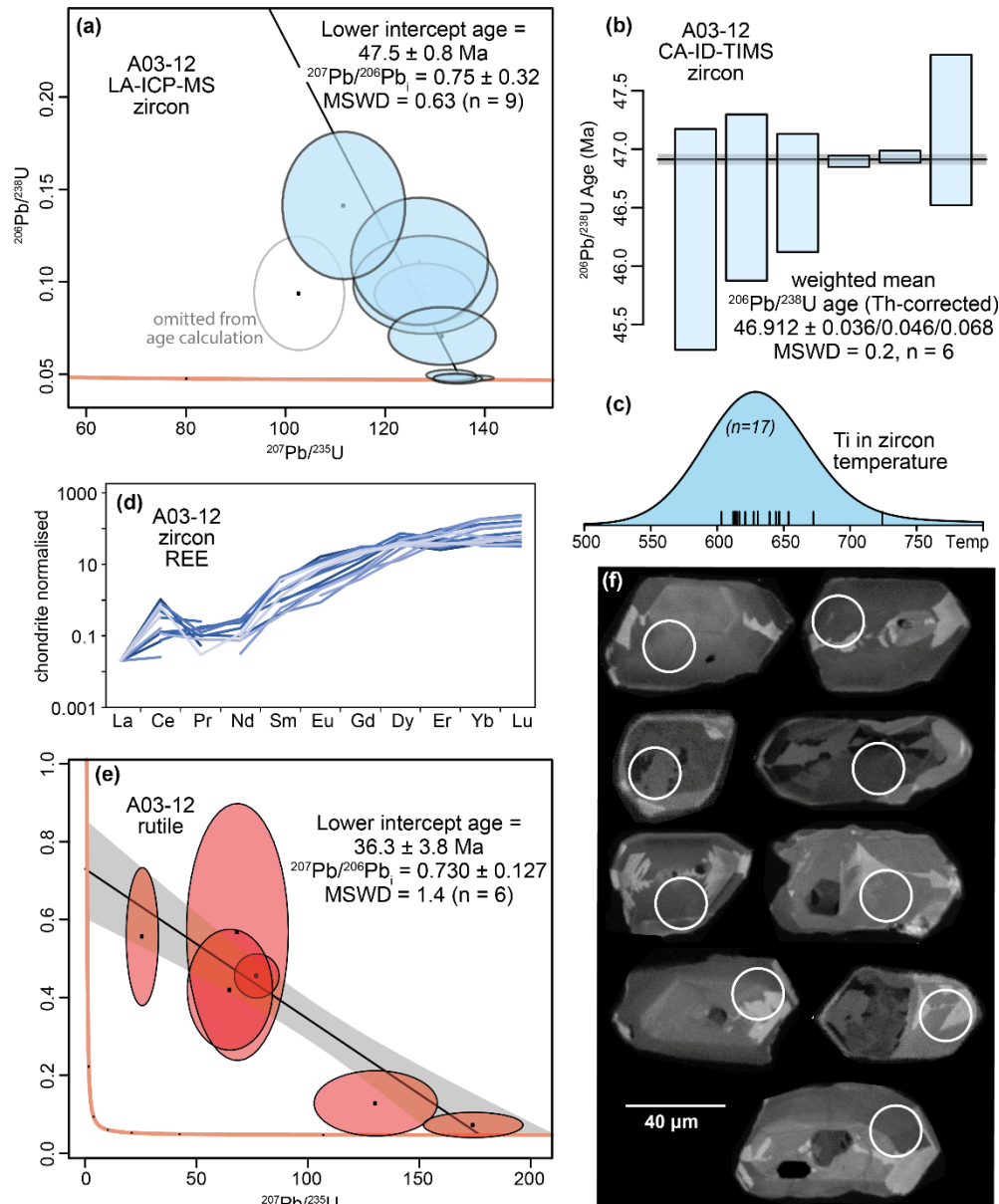
640   Figure 7. Mafic eclogite sample a03-12 a. Tera-Wasserburg plot of LA-ICP-MS U-Pb data for zircon,

641   with lower intercept $^{206}Pb/^{238}U$ age. b. Weighted mean $^{206}Pb/^{238}U$ (Th corrected) age of 6 zircon grains

642   using   CA-ID-TIMS.uncertainties   are   quoted   as   analytical   only/analytical+tracer-

643   calibration/analytical+tracer-calibration+decay-constant uncertainty. c. Histogram of Ti in zircon

644 temperatures. d. Sample a03-12 zircon chondrite-normalised REE data. e. Tera-Wasserburg plot of LA-
645 ICP-MS U-Pb data for rutile, with lower intercept $^{206}Pb/^{238}U$ age. f. Cathodoluminescence images of
646 zircon separates from sample a03-12. All box heights and uncertainty ellipses are 2σ uncertainties.
647

648 *4.3.2. Rutile*
649 Rutile grains in sample a03-12 show homogenous brightness in BSE with no indication of internal
650 zonation. The majority of analyses had Pb counts below detection, the remaining data comprise six
651 spots analysed across 6 grains. The analyses are distributed between the radiogenic and common lead
652 components, and using a free regression, yield a lower intercept age of 36.3 ± 3.8 (MSWD = 1.4; Fig.
653 7e).
654

655 **4.4. Summary and Interpretations**
656 *4.4.1. Puga Gneiss (sample 05-02)*
657 Zircon core ages of 482.0 ± 5.9 Ma in the Puga Gneiss are interpreted to represent the igneous
658 crystallisation age and are comparable with U-Pb zircon ages of 479 ± 1 Ma in both the Polokongka La
659 granite and the Puga Gneiss (Girard and Bussy, 1999). A monazite age of 473 ± 9 Ma in the Polokongka
660 La granite, interpreted to have formed during crystallisation of the granite (Bidgood et al., 2022), also
661 overlaps with the age of zircon crystallisation. Rim analyses of Ordovician zircon from the Puga Gneiss
662 yielded an age of 48.9 ± 1.2 Ma (LA-ICP-MS), which overlap with high precision CA-ID-TIMS zircon
663 age from mafic eclogite a03-12 (hosted within the gneiss), suggesting that zircon rims in the Puga gneiss
664 also grew at eclogite-facies conditions.
665

666 Xenotime is found exclusively in Puga Gneiss sample 05-02, in mica aggregates adjacent to the
667 corroded outer rim of a large garnet porphyroblast (Figs. 2 and 3). Breakdown of parts of the Mg-
668 enriched garnet rims, formed under peak eclogite-facies conditions (M2), liberated Y, which is
669 concentrated in garnet zones P2 and P3 (Fig. 3a), for xenotime growth. We therefore interpret the U-Pb
670 xenotime age in sample 05-02 (47.4 ± 1.4 Ma) as the age of initial garnet breakdown during
671 decompression. The xenotime age overlaps with the eclogite facies zircon rim age within the same
672 sample 05-02 (48.9 ± 1.2 Ma), as well as the precise eclogite-facies zircon CA-ID-TIMS age of mafic
673 eclogite sample a03-12 (46.912 ± 0.068 Ma), located within the same structural unit. This allows us to
674 assign the xenotime crystallization and garnet breakdown in the Puga Gneiss sample to the M3a
675 metamorphic assemblage, reflecting the earliest phase of decompression at eclogite facies conditions.
676

677 Rutile is present as inclusions within prograde (M1) to peak pressure (M2) garnets and the matrix of
678 the Puga Gneiss. Given that the peak temperature of the Tso Morari Complex (705-755°C, St-Onge et
679 al., 2013) is greater than the closure temperature of rutile at ~400 - 630 °C (Cherniak, 2000; Koojiman
680 et al., 2010; Mezger et al., 1989; Vry & Baker, 2006), which is dependent on cooling rate and grain size

681   (Zack and Koojiman, 2017; Oriolo et al., 2018), the U-Pb age of rutile can therefore be attributed to

682   cooling of the Puga Gneiss through the rutile closure temperature at 40.4 ± 1.1 Ma, after peak

683   temperature conditions.

684

685   *4.4.2. Retrogressed mafic eclogite (sample a03-12)*

686   LA-ICP-MS analyses of zircon from mafic eclogite sample a03-12 are entirely <50 Ma, and provide a

687   weighted mean age of 47.5 ± 1.7 Ma. Although a limited dataset (9 analyses), our result implies a single

688   population of metamorphic zircon, rather than preserving a protracted history of zircon growth. Flat

689   HREE profiles and the lack of an Eu anomaly in the core and mantle of zircon grains are indicative of

690   crystallisation in garnet-present, plagioclase-absent conditions, consistent with crystallisation in the

691   eclogite facies (Schaltegger et al., 1999; Rubatto, 2002; Rubatto and Hermann, 2003). The measured

692   zircon date is therefore interpreted to correspond to growth within the eclogite-facies. Ti in zircon

693   temperatures of 603 °C to 724 °C lie below the closer temperature of Ti in zircon (~ 900 °C, Watson et

694   al., 2006; Cherniak et al., 2007) and is therefore interpreted as the zircon crystallisation temperature.

695

696   The zircon CA-ID-TIMS data from mafic eclogite sample a03-12 are tightly clustered yielding a date

697   of 46.91 ± 0.068 Ma, which we interpret as the age of zircon growth at eclogite facies conditions (M1-

698   3a). We note that this interpretation is heavily weighted to only the two analyses of the most U-rich

699   zircon, excluding these analyses yields a weighted mean of 46.71 ± 0.33/0.38/0.38 Ma (MSWD = 1.04;

700   n=4) and is therefore within uncertainty of the original interpretation. Regardless of interpretation, the

701   uncertainty associated with the CA-ID-TIMS data is 1 to 2 orders of magnitude smaller than LA-ICPMS

702   U-Pb data and provides the most precise estimate of the timing of metamorphic zircon growth from Tso

703   Morari thus far. Additionally, even with the improved precision, the analyses and the lack of dispersion

704   indicated by their MSWDs suggests no measurable crystal to crystal variation at around the ~1 Myr

705   resolution.

706

707   Rutile is the peak titanium-bearing phase in mafic rocks during eclogite-facies metamorphism and is

708   present as inclusions in garnet (M1), as well as in the matrix (M2-3b). Peak temperature in the Tso

709   Morari Complex is estimated at 600 - 755°C (De Sigoyer et al., 2000; St-Onge et al., 2013), above the

710   predicted closure temperature of rutile at ~400 - 630 °C (Cherniak, 2000; Koojiman et al., 2010;

711   Mezger et al., 1989; Vry & Baker, 2006) which is dependent on cooling rate and grain size (Zack and

712   Koojiman, 2017; Oriolo et al., 2018). The U-Pb age of rutile can therefore be attributed to cooling

713   through this closure temperature range.

714

715

5. Metamorphism, deformation and geochronology of the Tso Morari Complex

Previous studies indicate that subduction, exhumation and emplacement of the Tso Morari Complex took place between c. 60 Ma and c. 7.5 Ma (Fig. 6), with exhumation to lower crustal conditions by 45.3 ± 1.1 Ma at an average rate of ~ 12 mm a^{-1} (St-Onge et al., 2013). The texture and composition of the mafic eclogites and Puga gneiss samples in this study collectively provide a record of initial exhumation from UHP eclogite-facies conditions, followed by exhumation through crustal conditions. Integrating this information with our new high-precision geochronology from a range of accessory phases which crystallized at different stages of metamorphism allows us to constrain the timing of mineral growth and fabric development with respect to the burial and exhumation of the Tso Morari Complex.

Evidence of prograde metamorphism to peak pressures (M1-2) is preserved within garnets from mafic eclogite and the Puga Gneiss, comparable to that observed in the eclogite studied by St-Onge et al (2013). The garnet-bearing Puga Gneiss, as represented by sample 05-02, is not typical of the host Puga Gneiss, which generally preserves only amphibolite-facies assemblages. The formation and preservation of garnet in this sample is therefore particularly valuable given that it records the same overall prograde compositional trends as seen in the Tso Morari eclogites. The analysed garnet (Fig. 3a,b) also contains complex deformation fabrics and inclusion suites, indicating that deformation and transformation of the original granite was already underway prior to garnet growth (M1) in at least part of the complex. Early fabrics are rarely preserved in the Tso Morari Complex, where the earliest stage of macroscopic deformation has been previously identified as the dominant top-to-the-east exhumation fabric within the Puga Gneiss, and is attributed to initial M3a exhumation from eclogite-facies conditions (Epard and Steck, 2008).

Our eclogite-facies zircon dates of 46.912 ± 0.068 Ma (CA-ID-TIMS) and 47.5 ± 1.7 Ma (LA-ICPMS) from a mafic eclogite overlap with our zircon rim and xenotime dates in the Puga Gneiss. We interpret this overlap as a record of the earliest phase of decompression at 630 °C and eclogite facies conditions, as recorded by the Ti in zircon temperatures and the partial breakdown of yttrium-bearing garnet rims. The crucial breakdown of the garnet rim zones and fracture-based alteration, with xenotime among its products, provides insight into the early exhumation history of these rocks that is not recorded elsewhere, but predates the Barrovian overprint of 7.0 - 8.4 kbar, 705 - 755 °C recorded at 45.3 ± 1.1 Ma and 43.3 ± 1.1 Ma by St-Onge et al. (2013).

750 The formation of quartz microstructures during high-temperature (> 530°C) dynamic recrystallisation

751 indicates that deformation took place during exhumation to crustal conditions (M3b). There is no

752 significant later overprinting of quartz deformation fabrics in Puga Gneiss samples from the core of the

753 dome (Bidgood, 2020), implying a lack of pervasive deformation below 530°C. Deformation therefore

754 occurred prior to cooling through the rutile closure temperature of ~630-400 °C (Cherniak, 2000; Li et

755 al., 2013; Mezger et al., 1989; Vry & Baker, 2006) at 40.4 ± 1.1 Ma and was ductile and pervasive. This

756 interpretation is confirmed by Dutta and Mukherjee (2021) who predict deformation temperatures >

757 600°C based on misorientation analysis and micro-textural evidences of incipient partial melting in the

758 Puga gneiss. Subsequent deformation during exhumation relating to doming and emplacement (M3c)

759 was not pervasive, with foliations and lineations developing at the margins of the dome, adjacent to the

760 normal sense shear zones (e.g. Zildat-Ribil fault, Epard and Steck, 2008; Bidgood, 2020; Dutta and

761 Mukherjee, 2021). The age of exhumation of the Tso Morari dome is recorded by the Ar-Ar muscovite

762 and biotite and apatite fission track dates of < 32.4 Ma (De Sigoyer et al., 2000; Schlup and Carter,

763 2003) which record cooling through the Ar closure temperatures of muscovite (~ 425°C, Harrison et

764 al., 2009), biotite (< 345°C, Harrison et al., 1985) and apatite (< 135°C, Warnock et al., 1997)

765 respectively.

766

6. Discussion

6.1. Continental subduction and exhumation in the NW Himalaya

769 Our petrographic correlation of zircon and xenotime ages with the M3a assemblage indicates that zircon

770 growth at ~ 47-46 Ma took place at subsolidus conditions during the earliest stages of decompression

771 from UHP conditions. These ages overlap with the zircon age distribution peak of 47-43 Ma recorded

772 by Donaldson et al. (2013). Considering their analytical scatter (i.e. MSWDs of 2.4 and 3.4) the

773 Donaldson et al. dates have reasonable agreement with our 47-46 Ma age, however, those data were

774 previously interpreted as a record of UHP metamorphism, starting at ~ 47 Ma. It is therefore necessary

775 to reassess the Donaldson et al. (2013) data in light of our new data and observations, as follows.

776 Subsolidus zircon growth requires a fluid phase to mediate the liberation of Zr from Zr-bearing phases

777 (ilm, ru, cpx, grt) (Chen et al., 2010; Kohn et al., 2015; Chen and Zhang, 2017; Skuzovatov et al., 2021).

778 The host rock in the Tso Morari complex is a dry granite with intruded mafic dykes (see Bidgood et al.,

779 2023) resulting in restricted opportunity for prograde/peak zircon growth. Palin et al. (2014) determined

780 that the first pulse of post-peak fluid in the eclogite facies relates to the destabilisation of talc and growth

781 of the coarse-grained amphiboles at ~ 23 kbar, followed by fluid infiltration from an external source at

782 ~ 19 kbar. Coarse-grained, zoned amphiboles are abundant in mafic eclogites from across the Tso

783 Morari Complex suggesting that post-peak eclogite facies hydration was a common and widespread

784 occurrence, aided further by exhumation-related deformation. These influxes of fluid during

785 exhumation, subsequent to a potentially dry spell at prograde to peak conditions, would have provided

786   conditions favourable for high concentrations of zircon growth. Consequently, we argue that the
787   breakdown of UHP garnet rims recorded by xenotime at 47.4 ± 1.4 Ma indicates that the zircon age
788   peak at 47 – 43 Ma of Donaldson et al. (2013), along with our own CA-ID-TIMS zircon age of 46.91 ±
789   0.068 Ma, reflects a pulse of zircon growth during the onset of exhumation from UHP conditions, aided
790   by the exhumation-driven liberation of fluids.

791   Based on the above conclusion, older dates in previous studies, including a 58 ± 2.2 Ma (n = 2) zircon
792   age from St-Onge et al (2013) and apparent older zircon dates (55 – 48 Ma) from Donaldson et al.
793   (2013), may record zircon growth during prograde to peak metamorphism. However, it is difficult to
794   place them in a robust context given: 1) the proportion of common lead for most of the analyses; 2) the
795   potential ablation of older zircon domains reflecting the protolith age; and 3) the lack of relationship
796   between textural location and REE chemistry (Fig. 8a). The nature of apparent younger common-lead
797   corrected dates from the Donaldson et al. (2013) dataset also remain uncertain for the same reasons;
798   younger dates could plausibly record continued zircon growth during decompression, but dates younger
799   than the ca. 40 Ma rutile age imply these may relate to analytical inaccuracies. Given that we consider
800   our xenotime date as a marker for the onset of UHP exhumation, we suggest that the Donaldson et al.
801   (2013) data reflect zircon growth due to fluid infiltration at and after 47 Ma.

802   Our new CA-ID-TIMS zircon age of 46.912 ± 0.068 Ma more closely and precisely correlates with ages
803   from zircon (46.4 ± 0.1 Ma – ID-TIMS; 46.2 ± 0.7 – SHRIMP, 46 ± 2 Ma - SIMS) and allanite (46.5
804   ± 1.0 Ma – ID-TIMS) in UHP assemblages from Kaghan, located 450 km to the west of Tso Morari
805   (Kaneko et al., 2003; Parrish et al., 2006; Zhang et al., 2022) (see Fig. 8). We do not think this is
806   coincidental; metamorphic P-T data from both of these units record similar prograde (up to UHP
807   metamorphism) and retrograde (including UHP exhumation and exhumation through the crust) P-T
808   paths. In Kaghan, coesite is found in thin metamorphic zircon rims in the felsic gneiss, indicating that
809   zircon crystallisation occurred at UHP conditions (Kaneko et al., 2003). In the Tso Morari Complex,
810   coesite is observed in the outermost rims of prograde garnets but has not yet been observed as inclusions
811   in zircon. Quartz microstructures after the presence of former coesite are also reported from the
812   Polokongka La Granite of the Tso Morari Complex (Bidgood et al., 2021). Based on these similarities,
813   we argue that the overlap in ages between Tso Morari and Kaghan indicates that UHP exhumation and
814   associated fluid flux at 47- 46 Ma was responsible for a ubiquitous pulse of zircon growth across the
815   NW Himalaya, occurring at the same time as or shortly after the achievement of maximum P and T
816   under UHP conditions. We suggest that the regional synchroneity between Tso Morari and Kaghan,
817   across a distance of ~450 km, reflects the scale at which slab dynamics control metamorphism and
818   exhumation with a subduction zone setting.

819   The mode of UHP exhumation is unclear from our data. Isothermal, triclinic deformation during
820   exhumation of the Tso Morari complex, as reported by Long et al. (2020) and Dutta and Mukherjee

821   (2021), is most compatible with the recirculation model and plunger model of Warren et al. (2008a,

822   2008b, 2008c). These models invoke the transport of crustal slices of the lower plate from UHP

823   pressures along the subduction interface, rather than wholesale exhumation of the subducting slab, and

824   can therefore occur independently from, and without need for slab break-off. The timing of slab break-

825   off cannot be resolved from our data and therefore remains debated, with estimates ranging widely

826   between ~50-10 Ma (see reviewed compilation of Garzanti et al., 2018).

827   Lastly, cooling through the rutile closure temperature took place ~ 3.7 Ma later in Tso Morari than

828   Kaghan (see Fig. 8). At face value, this implies a longer period of time between zircon growth and

829   exhumation through the rutile closure temperature for the Tso Morari Complex, relative to Kaghan.

830   However, uncertainties in the exact conditions of zircon growth and rutile closure temperature prevents

831   us from making any meaningful interpretation for the cause of this difference.
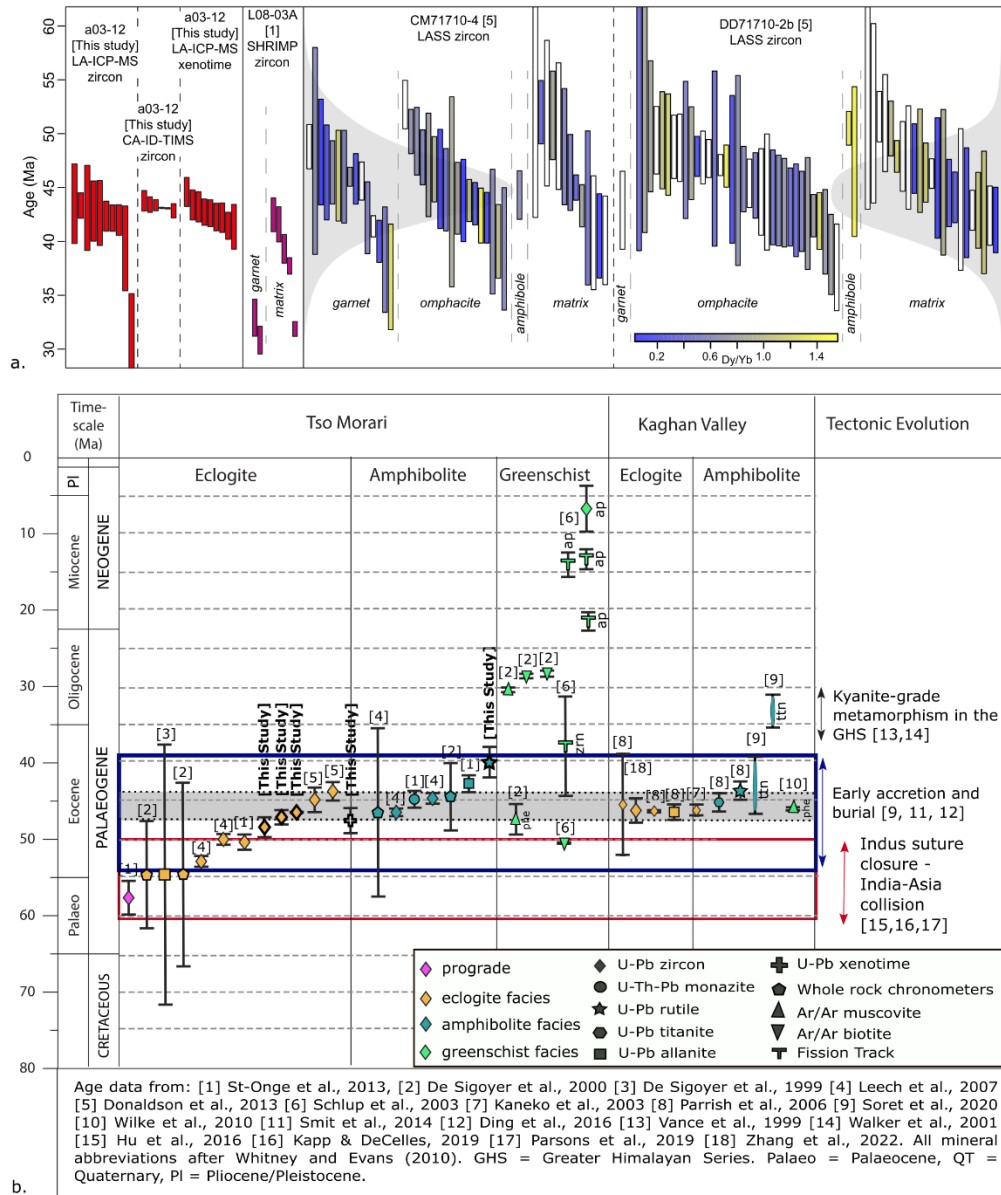
Figure 8: a. Zircon data for individual samples from this study, St-Onge et al., (2013) and Donaldson et al., (2013). Blue-yellow colour scale represents Dy/Yb. Solid colours do not contain individual REE spot data. Sample histograms shown in grey for Donaldson et al., (2013). b. Time chart for Tso Morari and Kaghan, after (Palin et al., 2012), comprising data from multiple sources, including this study.

6.2. Geodynamic significance of UHP exhumation during the Himalayan orogeny

Our data suggest that zircon crystallisation recorded in the Tso Morari complex and Kaghan at 47-46 Ma, corresponds to the onset of exhumation of Indian continental crust from UHP conditions. In the following sections, we consider the geodynamic significance of this event with respect to the wider

843   metamorphic, magmatic and plate kinematic evolution of the Himalayan orogeny and the India-

844   Australia-Eurasia plate network (Figs. 9 & 10).

6.2.1. UHP exhumation during the Himalayan orogeny

846   When placed in context with the bedrock record of collision, our constraints for the onset of UHP

847   exhumation in the NW Himalayan reveal how changes in subduction dynamics affected the structural,

848   magmatic, and metamorphic evolution of the Himalayan orogeny (Fig. 9).

849   In the lower plate (Indian crust), the onset of UHP exhumation at 47-46 Ma overlaps with the onset of

850   local prograde amphibolite facies, Barrovian-style metamorphism in the NW Himalaya at 47 Ma to 39

851   Ma (Soret et al., 2021) (Fig. 9a). This was followed by wide-spread amphibolite facies metamorphism

852   of the Himalayan metamorphic core (HMC) across the rest of the Himalaya during crustal thickening

853   of the HMC from ~41 Ma through to ~17 Ma (Fig. 9a) (Ambrose et al., 2015, Carosi et al., 2016,

854   Goscombe et al., 2018, Carosi et al., 2019, Mottram et al., 2019, Waters, 2019; Ji et al., 2024), whilst

855   high-pressure eclogite to granulite facies metamorphism of Indian lower crust is recorded in localized

856   occurrences across the orogen from 40 Ma to 25 Ma (Fig. 9a) (O'Brien, 2019a, Chen et al., 2022).

857   UHP exhumation at 47-46 Ma also overlaps with significant magmatic and metamorphic changes in the

858   upper plate of the orogen (Eurasian crust)(Fig. 9a; see also Fig. 10c for locations). Between 50 Ma and

859   40 Ma, isotopic signatures of magmatic rocks from the Kohistan-Ladakh batholith record increased

860   crustal contamination of arc magmatism (Fig. 9a) (Bouilhol et al., 2013, Jagoutz et al., 2019). Along

861   the Lhasa block, the Gangdese arc records adakite magmatism from ~48 Ma produced by melting of

862   the Tibetan lower crust (e.g., Searle et al., 2011, Guan et al., 2012, Ma et al., 2014), and the cessation

863   of subduction-related magmatism by ~40 Ma (Fig. 9a)(e.g., Zhu et al., 2019). At the same time, the

864   Lhasa block recorded high pressure-low temperature kyanite-grade partial melting associated with

865   deformation and crustal thickening at 44-32 Ma (Fig. 9a) (Zhang et al., 2010, Palin et al., 2014). Further

866   to the east, the Mogok metamorphic belt and Eastern Ophiolite Belt in Myanmar record sillimanite-

867   grade metamorphism between 48-22 Ma, which included a phase of granulite facies metamorphism

868   between 43-32 Ma (Fig. 9a) (Barley et al., 2003, Searle et al., 2007, Searle et al., 2017, Searle et al.,

869   2020, Lamont et al., 2021).

870   Collectively the structural, metamorphic, and magmatic changes recorded in both the lower and upper

871   plates of the Himalayan orogeny between ~50-40 Ma (Fig. 9a) reflect (1) a warming metamorphic

872   thermal gradient (e.g., Soret et al., 2021, Chen et al., 2022; Ji et al., 2024); (2) greater mechanical

873   coupling of the upper and lower plates resulting in increased crustal shortening and thickening; and (3)

874   a greater contribution of Indian continental crustal material to upper plate magmatism. These

875   phenomena are best explained by a reduction in the dip of the subducting Indian plate beneath Eurasia

876   during that time (Fig. 10a-b) (e.g., Soret et al., 2021, Chen et al., 2022; Ji et al., 2024). We attribute this

877   to the early stages of the India-Asia collision *sensu stricto* (i.e., second collision of the Himalayan

878 orogeny), whereby the positive buoyancy of the Indian continental crust stalled subduction of the Indian

879 plate beneath the Eurasian margin (Fig. 9b).

880 *6.2.2. A shift in orogenic regimes*

881 UHP exhumation at 47-46 Ma marks a significant geodynamic shift in the orogenic regime of the

882 collision zone (Figs. 9b, 10a,b). Prior to this time, India-Asia convergence was accommodated by

883 subduction of Indian and/or Neotethys oceanic lithosphere beneath Eurasian. Then, following the India-

884 Asia continent-continent collision *sensu stricto* by 47 Ma, the reduced dip of the Indian slab increased

885 the mechanical coupling between upper and lower plates and the component of convergence

886 accommodated by crustal shortening. This switch in mode of convergence can be viewed as a shift in

887 the orogenic regime of the collision zone (cf. Cawood et al., 2009) from (1) an *accretionary orogen*, in

888 which India-Asia convergence was driven and accommodated by subduction of Indian and/or Neotethys

889 oceanic lithosphere (Fig. 10a); to (2) a *collisional orogen*, in which India-Asia convergence was

890 accommodated by crustal shortening (*e.g.,* Replumaz et al., 2014; Parsons et al., 2021; Chen et al.,

891 2022), and driven by northeastward subduction of Indian-Australian oceanic lithosphere beneath SE

892 Asia, further to the east (Fig. 10b) (e.g., Li et al., 2008; Capitanio et al., 2015; Parsons et al., 2021, Bose

893 et al., 2023). The onset of UHP exhumation at 47-46 Ma therefore timestamps the change in orogenic

894 regime of the India-Asia collision zone from an *accretionary orogen* to a *collision orogen* (*cf.* Cawood

895 et al., 2009) (Fig. 9b).

896 *6.3.2. Implications for models of the Himalayan orogeny and the India-Asia continent-continent*

897 *collision (sensu stricto)*

898 We interpret the onset of the India-Asia collision (sensu stricto) to occur at ~50-47 Ma, based on (1)

899 our constraint for the onset of UHP exhumation at 47-46 Ma; (2) a reduction in Indian plate velocity

900 starting at ~50 Ma (Fig. 9c); (3) plate reconstructions of the restored Indian and Eurasian margins at

901 50-45 Ma (Fig. 10b) (Replumaz et al., 2014; Parsons et al 2021); and (4) changes in the magmatic and

902 metamorphic evolution of the Eurasian margin (upper plate) between 50-40 Ma (listed above)(Fig. 9a).

903 In the context of our data, single collision models initiating at ~60 Ma (e.g., Hu et al., 2016, Ingalls et

904 al., 2016) would require ~14 Myrs of uninterrupted continental subduction prior to UHP exhumation of

905 Tso Morari at 47-46 Ma. This equates to wholesale subduction of a 2500 x 2000 km area of Indian

906 continental lithosphere. This scenario remains highly disputed and is not discussed further as it is yet to

907 be shown that such extreme volumes of continental subduction are feasible or sustainable (Afonso and

908 Zlotnik, 2011, Ingalls et al., 2016, van Hinsbergen et al., 2019, Parsons et al., 2020).

909 In the context of double-collision models for the Himalayan orogeny, prograde to peak metamorphism

910 of the Tso Morari complex between 60-50 Ma (Leech et al., 2007; St-Onge et al., 2013; Donaldson et

911 al., 2013), as well as Barrovian metamorphism of the North Himalayan gneiss domes between 56-54

912   Ma (Smit et al., 2014, Ding et al., 2016), may be explained by initial burial of the NW Himalaya during

913   the first collision event of the Himalayan orogeny (Fig. 9a) (first collision began at ~61 Ma, see

914   introduction for definitions). Our new data do not permit us to constrain the validity of the opposing

915   hypotheses for first collision beyond that which is already discussed in recent reviews (e.g., Kapp &

916   DeCelles, 2019; van Hinsbergen et al., 2019; Parsons et al., 2020). However, we note that models

917   proposing first collision of the Himalayan orogeny between India and an equatorial intra-oceanic arc at

918   ~61 Ma require two collisions at two separate subduction zones (an intra-oceanic subduction zone and

919   a continental margin subduction zone) and therefore require two slab break-off events. We are unaware

920   of any studies (including our own), which present bedrock evidence for more than one break-off event
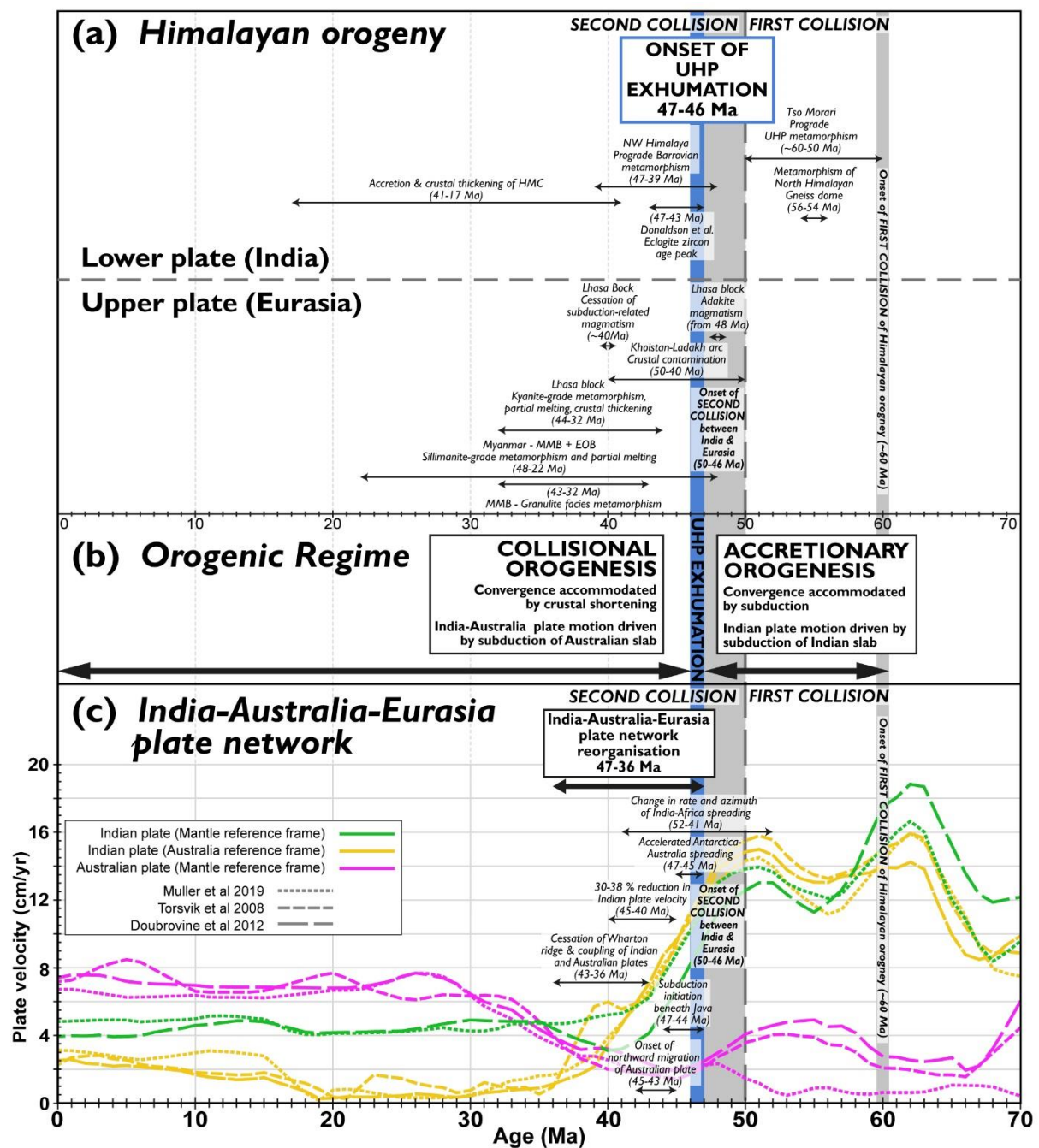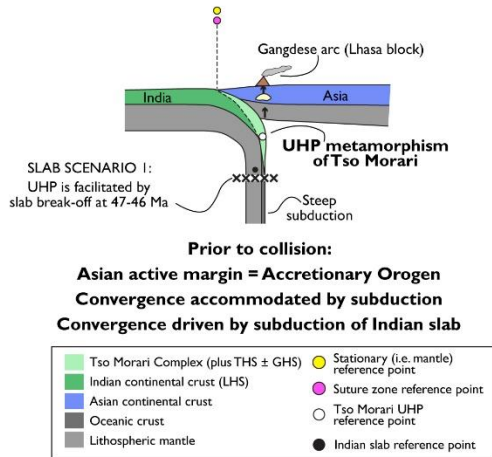
921   during the Himalayan orogeny.

Figure 9. UHP exhumation at 47-46 Ma and its temporal relationship with the metamorphic, magmatic, and plate kinematic evolution of the Himalayan orogeny and India-Australia-Eurasia plate network. (a) Metamorphic and magmatic events in the Himalayan orogeny. (b) Orogenic regime of the Himalayan orogeny: onset of UHP exhumation marks the transition from an accretionary orogen to a collisional orogen (c.f., Cawood et al., 2009). (c) Reorganization of the India-Australia-Eurasia plate network at 47-36 Ma with plate velocity profiles for the Indian and Australian plates (Torsvik et al., 2008, Doubrovine et al., 2012, Müller et al., 2019) plotted using GPlates (Müller et al., 2018). Data sources for events in (a) and (c) are cited in the main text. (c) is modified after Parsons et al. (2021). EOB – Eastern Ophiolite Belt; HMC – Himalayan Metamorphic core; MMB – Mogok Metamorphic Belt.

(a) 50-47 Ma: Onset of India-Asia collision

Gangdese arc (Lhasa block)

India Asia

UHP metamorphism
of Tso Morari

SLAB SCENARIO 1:
UHP is facilitated by
slab break-off at 47-46 Ma

xxxxx

Steep
subduction

Prior to collision:
Asian active margin = Accretionary Orogen
Convergence accommodated by subduction
Convergence driven by subduction of Indian slab

Tso Morari Complex (plus THS ± GHS) — Stationary (i.e. mantle) reference point
Indian continental crust (LHS) — Suture zone reference point
Asian continental crust — Tso Morari UHP reference point
Oceanic crust
Lithospheric mantle — Indian slab reference point

(b) 47-46 Ma and younger

North migration of
collision zone

Crustal thickening &
Barrovian metamorphism

Continental contamination
of arc magmatism + adakite produced
by lower crustal melting

Shallowing
of slab dip

UHP exhumation of
Tso Morari

xxxxx

SLAB SCENARIO 2 (DASHED LINES):
Slab break-off occurs later (post-40 Ma)
Buoyancy of Indian continent drives UHP
exhumation and results in lateral slab dragging

India-Asia collision zone = Collisional Orogen
Convergence accommodated by crustal shortening
± continental subduction
Convergence driven by subduction of Australian slab

(c)

47-46 Ma:
ONSET OF UHP EXHUMATION
MARKS CHANGE IN
SUBDUCTION DYNAMICS
OF INDIA-ASIA COLLISION

46 Ma Reconstruction:
Eocene plate network
reorganization

Triggered by changes in
subduction dynamics
forced by onset of the
India-Asia collision

EURASIA

INDIA

45-40 Ma: 30%–38%
reduction of IND
plate speed

47-44 Ma: Onset of
subduction of the AUS
plate beneath Java (ja)

41 Ma: Southwestward
jump of the Central
India ridge (CIR)

AFR

43-36 Ma: Cessation
of Wharton Ridge
(WR) & coupling of
IND & AUS plates

IND

52-41 Ma: Clockwise rotation
and reduction in rate of
IND-AFR spreading azimuth

45-43 Ma: Onset of
northward motion
of AUS plate

AUS

ANT

47-45 Ma:
Acceleration of
AUS-ANT plate
spreading

932

933 Figure 10. The geodynamic significance of UHP exhumation for orogenesis and plate tectonics. (a-b)
934 Schematic cartoon section of the India-Asia collision showing the postulated shallowing of Indian slab
935 dip (e.g., Chen et al 2022), marked by the onset of UHP exhumation at 47-46 Ma (not to scale). (a)
936 Steep subduction and UHP metamorphism during onset of the India-Asia collision (~50-47 Ma). Prior
937 to collision, the Asian active continental margin represented an Accretionary Orogen (c.f. Cawood et
938 al., 2009) in which convergence was driven and accommodated by subduction of the Indian and/or
939 Neotethys slab. (b) UHP exhumation and slab shallowing starting at 47-46 Ma, in response to the

940 positive buoyancy of Indian continental crust following the onset of continental collision. The impacts

941 of the reduced slab dip are annotated on (b), showing an increase in crustal shortening, Barrovian

942 metamorphism, crustal contamination of arc magmatism and lower crustal melting of the Gangdese arc

943 to produce adakite. The collision zone represents a Collisional Orogen (c.f. Cawood et al., 2009),

944 whereby convergence is accommodated by crustal shortening ± continental subduction and driven by

945 subduction of the Australian slab to the east (see discussion). Two alternative slab break-off scenarios

946 are presented. Slab Scenario 1 (presented in (a)): UHP exhumation and slab dip shallowing occurred in

947 response to slab break-off at 47-46 Ma. Slab Scenario 2 (presented in (b)): Alternatively, UHP

948 exhumation occurred via detachment of the Tso Morari complex from the Indian slab, whilst the

949 buoyancy of the Indian continental crust resulted in lateral slab dragging, overturning of the trailing

950 oceanic slab and reduction in slab dip (see Parsons et al., 2021 for further discussion of lateral slab

951 migrations during the India-Asia collision), with slab break-off occurring at a later time (see discussion).

952 (c) 46 Ma plate reconstruction showing tectonic events of the Eocene plate network reorganization,

953 triggered by changes in the subduction dynamics of the India-Asia collision. UHP exhumation at 47-46

954 Ma provide a precise timestamp linking changes in the subduction dynamics of the India-Asia collision

955 zone to plate kinematic changes of the wider plate network. Reconstruction drawn from Müller et al.

956 (2019) using GPlates (Müller et al., 2018), with Greater India and Eurasian margin subduction zone

957 outlines constrained by Parsons et al. (2020; 2021). Thick dashed black lines show present day locations

958 of the Indus Suture Zone (ISZ) and Main Frontal Thrust (MFT) of the Himalayan orogen, , requiring

959 1000-2000 km of crustal shortening since ~47-46 Ma (Parsons et al., 2021). Abbreviations: AFR –

960 African plate; ANT – Antarctic plate; AUS – Australian plate; CIR – Central Indian ridge; GI – Greater

961 India; IND – Indian plate; ISZ – Indus Suture Zone; ja - Java; khl – Khoistan-Ladakh block; lh – Lhasa

962 block; MFT – Main Frontal Thrust; mk – Mogok metamorphic belt; wb - West Burma block; WR –

963 Wharton ridge

964 **6.2.4. UHP exhumation during Eocene plate network reorganization**

965 From a plate-kinematic perspective (Fig. 10c), UHP exhumation at 47-46 Ma coincides with a

966 significant reorganisation of the India-Eurasia-Australia plate network during the mid-Eocene (e.g.,

967 Patriat and Achache, 1984, Gibbons et al., 2015, Parsons et al., 2021). Key events during the

968 reorganization (Fig. 10c) included (1) a deceleration of Indian plate motion by 30%–38% between 45-

969 40 Ma (Molnar and Stock, 2009); (2) reduction in spreading rate and clockwise rotation of spreading

970 azimuth between India and Africa between 52-41 Ma (Patriat and Achache, 1984, Cande et al., 2010),

971 followed by southwest jump of the Central India spreading ridge at ~41 Ma (Torsvik et al., 2013); (3)

972 coupling of the Indian and Australian plates following a cessation of spreading on intervening Wharton

973 ridge at ~43-36 Ma (Jacob et al., 2014, Gibbons et al., 2015); (4) onset of northward motion of the

974 Australian plate at ~45-43 Ma, after being stationary since the mid-Cretaceous (Torsvik et al., 2008,

975 Müller et al., 2019); (5) onset of subduction of the Australian plate beneath Java at 47-44 Ma (Smyth

976 et al., 2008); and (6) acceleration of plate spreading between the Australian and Antarctic plates at ~47-
977 45 Ma (Torsvik et al., 2008, Eagles, 2019).

978 Plate reconstructions and mantle tomographic analyses propose that this reorganisation occurred in
979 response to the India-Asia collision (Replumaz et al. 2014; Gibbons et al., 2015, Parsons et al., 2021);
980 however, these studies lacked an unambiguous and precise marker linking the bedrock record of the
981 collision to plate network reorganization. Crucially, our precise age constraint for the onset of UHP
982 exhumation at 47-46 Ma corroborates those previous studies by demonstrating a viable, causative link
983 between changes in the subduction dynamics of the India-Asia collision zone starting at 47-46 Ma (Fig.
984 9) and the resulting mid-Eocene plate network reorganization that immediately followed (Fig. 10c). Our
985 synthesis of the bedrock record of metamorphism and magmatism during the Himalayan orogeny
986 demonstrate that UHP exhumation was rapidly, and in some places immediately, followed by
987 widespread, hotter, amphibolite facies metamorphism (Fig. 9a), which we attribute to shallowing and
988 underthrusting of the Indian plate beneath Eurasia. Consequently, we argue that our new
989 geochronological constraints not only date the onset of UHP exhumation in the NW Himalaya, but also
990 date the changes in subduction dynamics of the collision zone that triggered the Eocene plate network
991 reorganization.

992

993 **6.3. The geodynamic significance of UHP exhumation for orogenesis and plate tectonics**

994

995 Our study demonstrates how our understanding of the bedrock record of continental collisions may be
996 enriched by placing it within the context of plate kinematics. At the same time, the bedrock record
997 provides a crucial means of ground truthing lithospheric- to planetary-scale models of plate tectonics
998 and mantle geodynamics. Further understanding may therefore be gained through new applications of
999 similar integrated approaches to other collision zones.

1000 Multiple examples of HP and UHP metamorphism are recorded across much of SE Asia during the
1001 Early to Late Cretaceous, but their timing and tectonic significance is poorly constrained. This
1002 metamorphism broadly overlaps with multiple terrane accretion events from the region (e.g., Woyla,
1003 Southwest Borneo, and Argoland blocks Hall, 2012, Morley, 2012, Metcalfe, 2021, Advokaat and van
1004 Hinsbergen, 2024, van de Lagemaat and van Hinsbergen, 2024), as well as a previously recognised
1005 plate network reorganization at ~110-100 Ma (Matthews et al., 2012, Müller et al., 2016). Detailed
1006 petrochronology studies of these occurrences of HP/UHP metamorphism are yet to be conducted but
1007 may provide important constraints for plate reconstructions and orogenic models of SE Asia which
1008 continue to be debated and revised (e.g., Hall, 2012, Morley, 2012, Metcalfe, 2021, Advokaat and van
1009 Hinsbergen, 2024, van de Lagemaat and van Hinsbergen, 2024).

1010 Further back in time, there are many examples HP and UHP metamorphic rocks associated with the
1011 Palaeozoic tectonic evolution of the Rheic and Iapetus Oceans and related collisional events including
1012 the Caledonian, Scandian, and Grampian orogenies (see review of Domeier, 2016). The tectonic and
1013 geodynamic significance of these HP/UHP rocks is often unclear. Integrated petrochronology-plate
1014 kinematic analyses of these rocks may better constrain both the tectonometamorphic evolution of these
1015 HP/UHP metamorphic events and the plate kinematic evolution of the surrounding plate network (e.g.,
1016 Gilotti et al., 2008, Hacker et al., 2010, Bottrill et al., 2014, Domeier, 2016). Whilst plate reconstructions
1017 of pre-Jurassic events are less well constrained than those of younger ages, integration of plate
1018 kinematics and bedrock dataset still has potential to reveal new information for older tectonic events
1019 that would remain otherwise hidden when conducting either discipline (bedrock analysis or plate
1020 reconstruction modelling) in isolation.

1021

1022 7. Summary

1023 By associating accessory phase ages with distinct metamorphic assemblages, and combining both high
1024 precision and high spatial resolution techniques, we demonstrate that the phase of peak zircon
1025 crystallization recorded in the Tso Morari complex at 47-46 Ma, corresponds to the onset of exhumation
1026 from UHP conditions. This study also describes the record of subduction-related major and accessory
1027 mineral growth preserved in a rare garnet-bearing Puga Gneiss, which records a part of the P-T-t history
1028 not preserved elsewhere. Zircon from a mafic eclogite have a U-Pb CA-ID-TIMS age of 46.912 ± 0.068
1029 Ma (2σ) and an LA-ICPMS age of 47.5 ± 1.7 Ma, with REE profiles indicative of zircon crystallization
1030 at eclogite facies conditions. Those ages overlap with zircon rim ages (48.9 ± 1.2 Ma, LA-ICP-MS) and
1031 xenotime ages (47.4 ± 1.4 Ma; LA-ICP-MS) from the hosting Puga gneiss, which grew during
1032 breakdown of UHP garnet rims, as indicated by garnet element maps. Subsequent exhumation through
1033 the rutile closure temperature to crustal conditions is constrained by new dates of 40.4 ± 1.7 Ma and
1034 36.3 ± 3.8 (2σ LA-ICP-MS).

1035 The overlap between our mafic eclogite zircon ages and our xenotime-UHP garnet break down ages,
1036 indicate that the pulse of zircon growth recorded in the Tso Morari complex at 47-46 Ma (e.g.,
1037 Donaldson et al., 2013) took place as a result of fluid infiltration at the onset of exhumation from UHP
1038 conditions, rather than as a result of peak UHP metamorphism. These ages from Tso Morari overlap
1039 with U-Pb ID-TIMS, SHRIMP, and SIMS analyses of zircon from eclogite-facies mafic rocks in
1040 Kaghan and Naran, ~450-480 km to west of Tso Morari, which yielded ages of 46.4 ± 0.1 Ma, $46.2 \pm$
1041 0.7 Ma, and 46 ± 2 Ma, respectively (Kaneko et al., 2003; Parrish et al., 2006; Zhang et al., 2022). We
1042 interpret this overlap as an indication that exhumation from UHP conditions occurred synchronously at
1043 46-47 Ma across the whole of the NW Himalaya.

Integration of our new ages plus previously published ages from the NW Himalaya with existing metamorphic, magmatic, and plate kinematic constraints demonstrates that UHP exhumation at 47-46 Ma occurred in response to changes in subduction dynamics following the onset of the India-Asia collision (*sensu stricto*) between 50-47 Ma. Our data suggest that UHP exhumation was rapidly and in some places immediately followed by widespread, hotter, amphibolite facies metamorphism which we attribute to buoyancy-driven shallowing and under thrusting of the continental Indian slab beneath Eurasia beginning at 47-46 Ma. At a broader perspective, these changes in subduction dynamics and convergence mechanisms of the Himalayan orogeny (Fig. 9a-b) also impacted the geodynamics and kinematics of the encompassing tectonic plate network.

Our new data from Tso Morari demonstrably tie the bedrock record of the Himalayan orogeny to slab dynamics and plate kinematics of the collision zone. Continent-continent collision of India and Asia at 50-47 Ma not only provided the trigger for UHP exhumation, but also resulted in, (1) significant changes in the metamorphic and magmatic evolution of the Himalayan orogen (Fig. 9a); (2) the transition of the Himalaya from an accretionary orogen to a collisional orogen (Fig. 9b); and (3) a significant reorganisation of the wider India-Eurasia-Australia plate network (Fig. 9c). Therefore, our new constraints not only date the onset of UHP exhumation in the NW Himalaya, but also date changes in subduction dynamics of the collision zone that triggered the Eocene plate network reorganization. As a proof-of-concept, our study demonstrates the value of integrated bedrock-plate kinematic approaches, which ultimately lead to a more holistic and accurate understanding how bedrock geology and plate tectonics are linked across subgrain to planetary scales.

8. Supporting Information

The EPMA, LA-ICPMS and ID-TIMS data used for geochemistry analysis and U-Pb dating in this study has been uploaded to the Mendeley data repository with a DOI and an open access license CC BY 4.0. EPMA data DOI: 10.17632/vcfbxm6h9f.1. Geochronology data DOI: 10.17632/t5fd58m67p.1.

    8.1. Supporting Information 1. Geochronology of the northwest Himalaya
       8.1.1.   Table A1: Published geochronology results from Tso Morari and Kaghan.

9. Acknowledgements

10. References

Advokaat, E.L. & van Hinsbergen, D.J.J. 2024. Finding Argoland: Reconstructing a microcontinental archipelago from the SE Asian accretionary orogen. Gondwana Research, 128, 161-263.

Afonso, J.C. & Zlotnik, S. 2011. The Subductability of Continental Lithosphere: The Before and After Story. Arc-Continent Collision. Berlin, Heidelberg: Springer Berlin Heidelberg. 53-86.

Ambrose, T.K., Larson, K.P., Guilmette, C., Cottle, J.M., Buckingham, H. & Rai, S. (2015). Lateral extrusion, underplating, and out-of-sequence thrusting within the Himalayan metamorphic core, Kanchenjunga, Nepal. Lithosphere, 7, 441-464. https://doi.org/10.1130/L437.1

An, W., Hu, X., Garzanti, E., Wang, J.-G. & Liu, Q. (2021). New Precise Dating of the India-Asia Collision in the Tibetan Himalaya at 61 Ma. Geophysical Research Letters, 48, e2020GL090641.

Babist, J., Handy, M. R., Konrad-Schmolke, M., & Hammerschmidt, K. (2006). Precollisional, multistage exhumation of subducted continental crust: The Sesia Zone, western Alps. Tectonics, 25(6). https://doi.org/10.1029/2005TC001927

Barley, M.E., Pickard, A.L., Zaw, K., Rak, P. & Doyle, M.G. (2003). Jurassic to Miocene magmatism and metamorphism in the Mogok metamorphic belt and the India-Eurasia collision in Myanmar. Tectonics, 22. https://doi.org/10.1029/2002TC001398

Beaumont, C., Jamieson, R. A., Butler, J. P., & Warren, C. J. (2009). Crustal structure: A key constraint on the mechanism of ultra-high-pressure rock exhumation. In Earth and Planetary Science Letters (Vol. 287, Issue 1). https://doi.org/10.1016/j.epsl.2009.08.001

Bidgood, A. K. (2020) The Petrology and Transformation History of Continental Crust in the Tso Morari Complex, Ladakh, Himalaya. University of Oxford. Available at: https://ora.ox.ac.uk/objects/uuid:966a9121-82fc-4567-afbf-2bbcd55de04e.

Bidgood, A. K., Parsons, A. J., Lloyd, G. E., Waters, D. J., & Goddard, R. M. (2021). EBSD-based criteria for coesite-quartz transformation. Journal of Metamorphic Geology, 39(2), 165–180. https://doi.org/10.1016/j.jsg.2018.06.012

1108   Bidgood, A.K., Waters, D.J., Dyck, B.J. & Roberts, N.M.W. (2023). The emplacement, alteration,
1109   subduction and metamorphism of metagranites from the Tso Morari Complex, Ladakh
1110   Himalaya. Mineralogical Magazine, 87, 40-59. https://doi.org/10.1180/mgm.2022.121

1111   Bingen, B., Austrheim, H., & Whitehouse, M. (2001). Ilmenite as a source for zirconium during high-
1112   grade metamorphism? Textural evidence from the Caledonides of western Norway and
1113   implications for zircon geochronology. Journal of Petrology, 42(2), 355–375.
1114   https://doi.org/10.1093/petrology/42.2.355

1115   Bose, S., Schellart, W.P., Strak, V., Duarte, J.C. & Chen, Z. (2023). Sunda subduction drives ongoing
1116   India-Asia   convergence.   Tectonophysics,   849,   229727.
1117   https://doi.org/10.1016/j.tecto.2023.229727

1118   Bottrill, A.D., van Hunen, J., Cuthbert, S.J., Brueckner, H.K. & Allen, M.B. (2014). Plate rotation
1119   during continental collision and its relationship with the exhumation of UHP metamorphic
1120   terranes: Application to the Norwegian Caledonides. Geochemistry, Geophysics, Geosystems,
1121   15, 1766-1782.

1122   Bouilhol, P., Jagoutz, O., Hanchar, J.M. & Dudas, F.O. (2013). Dating the India–Eurasia collision
1123   through arc magmatic records. Earth and Planetary Science Letters, 366, 163-175.
1124   https://doi.org/10.1016/j.epsl.2013.01.023

1125   Boutelier, D., & Cruden, A. R. (2018). Exhumation of (U) HP/LT rocks caused by diachronous slab
1126   breakoff.   Journal   of   Structural   Geology,   117,   251–255.
1127   https://doi.org/10.1016/j.jsg.2018.06.012

1128   Brun, J.-P. & Faccenna, C. (2008). Exhumation of high-pressure rocks driven by slab rollback. Earth
1129   and Planetary Science Letters, 272, 1-7. https://doi.org/10.1016/j.epsl.2008.02.038

1130   Buchs, N. and Epard, J.L., 2019. Geology of the eastern part of the Tso Morari nappe, the Nidar
1131   Ophiolite and the surrounding tectonic units (NW Himalaya, India). Journal of Maps, 15(2),
1132   pp.38-48. https://doi.org/10.1080/17445647.2018.1541196

1133   Burg, J.-P. & Bouilhol, P. (2019). Timeline of the South Tibet – Himalayan belt: the geochronological
1134   record of subduction, collision, and underthrusting from zircon and monazite U–Pb ages.
1135   Canadian Journal of Earth Sciences, 56, 1318-1332. https://doi.org/10.1139/cjes-2018-0174

1136   Burov, E., Francois, T., Agard, P., Le Pourhiet, L., Meyer, B., Tirel, C., Lebedev, S., Yamato, P. &
1137   Brun, J.-P. (2014). Rheological and geodynamic controls on the mechanisms of subduction and
1138   HP/UHP exhumation of crustal rocks during continental collision: Insights from numerical
1139   models. Tectonophysics, 631, 212-250. https://doi.org/10.1016/j.tecto.2014.04.033

1140   Capitanio, F.A., Replumaz, A. & Riel, N. (2015). Reconciling subduction dynamics during Tethys
1141   closure with large-scale Asian tectonics: Insights from numerical modelling. Geochemistry,
1142   Geophysics, Geosystems, 16(3), pp.962-982. https://doi.org/10.1002/2014GC005660

1143   Cande, S.C., Patriat, P. & Dyment, J. (2010). Motion between the Indian, Antarctic and African plates
1144   in the early Cenozoic. Geophysical Journal International, 183, 127-149.

1145   Capitanio, F.A., Replumaz, A. & Riel, N. (2015). Reconciling subduction dynamics during Tethys
1146   closure with large-scale Asian tectonics: Insights from numerical modeling. Geochemistry,
1147   Geophysics, Geosystems, 16, 962-982

1148   Carosi, R., Montomoli, C., Iaccarino, S., Massonne, H.-J., Rubatto, D., Langone, A., Gemignani, L. &
1149   Visonà, D. (2016). Middle to late Eocene exhumation of the Greater Himalayan Sequence in
1150   the Central Himalayas: Progressive accretion from the Indian plate. GSA Bulletin, 128, 1571-
1151   1592. https://doi.org/10.1130/B31471.1

1152   Carosi, R., Montomoli, C., Iaccarino, S. & Visonà, D. (2019). Structural evolution, metamorphism and
1153   melting in the Greater Himalayan Sequence in central-western Nepal. Geological Society,
1154   London, Special Publications, 483, 305-323. https://doi.org/10.1144/SP483.3

1155   Cawood, P.A., Kröner, A., Collins, W.J., Kusky, T.M., Mooney, W.D. & Windley, B.F. (2009).
1156   Accretionary orogens through Earth history. Geological Society, London, Special Publications,
1157   318, 1-36. https://doi.org/10.1144/SP318.1

1158   Chatterjee, N., & Jagoutz, O. (2015). Exhumation of the UHP Tso Morari eclogite as a diapir rising
1159   through the mantle wedge. Contributions to Mineralogy and Petrology, 169(1), 3.
1160   http://doi.org/10.1007/s00410-014-1099-y

1161   Chen, R.X. and Zheng, Y.F., (2017). Metamorphic zirconology of continental subduction
1162   zones. Journal   of   Asian   Earth   Sciences, 145,   pp.149-176.
1163   https://doi.org/10.1016/j.jseaes.2017.04.029

1164   Chen, S., Chen, Y., Guillot, S. & Li, Q. (2022). Change in Subduction Dip Angle of the Indian
1165   Continental Lithosphere Inferred From the Western Himalayan Eclogites. Frontiers in Earth
1166   Science, 9. https://doi.org/10.3389/feart.2021.790999

1167   Chen, R. X., Zheng, Y. F., & Xie, L. (2010). Metamorphic growth and recrystallization of zircon:
1168   Distinction by simultaneous in-situ analyses of trace elements, U–Th–Pb and Lu–Hf isotopes
1169   in zircons from eclogite-facies rocks in the Sulu orogen. Lithos, 114(1–2), 132–154.
1170   https://doi.org/10.1016/J.LITHOS.2009.08.006

1171   Cherniak, D. J. (2000). Pb diffusion in rutile. Contributions to Mineralogy and Petrology, 139(2), 198–
1172   207. https://doi.org/10.1007/PL00007671

1173   Cherniak, D., Watson, E. and Wark, D. (2007) Ti diffusion in quartz, Chemical Geology, 236(1–2), pp.
1174   65–74. https://doi.org/10.1016/j.chemgeo.2006.09.001

1175   Condon, D. J., Schoene, B., McLean, N. M., Bowring, S. A., & Parrish, R. R. (2015). Metrology and
1176   traceability of U–Pb isotope dilution geochronology (EARTHTIME Tracer Calibration Part I).
1177   Geochimica et Cosmochimica Acta, 164, 464–480.
1178   https://doi.org/10.1016/J.GCA.2015.05.026

1179   Cottle, J. M., Jessup, M. J., Newell, D.L., Horstwood, M. S., Noble, S. R., Parrish, R. R., Waters, D. J.,
1180   & Searle, M. P. (2009). Geochronology of granulitized eclogite from the Ama Drime Massif:
1181   Implications for the tectonic evolution of the South Tibetan Himalaya. Tectonics, 28(1).
1182   https://doi.org/10.1029/2008TC002256

1183   de Sigoyer, J;, Chavagnac, V., & Blichert-Toft, J. (2000). Dating the Indian continental subduction and
1184   collisional thickening in the northwest Himalaya: Multichronology of the Tso Morari eclogites.
1185   Geology, 28(6), 487–490. https://doi.org/10.1130/0091-
1186   7613(2000)28<487:DTICSA>2.0.CO;2

1187   de Sigoyer, J, & Guillot, S. (1997). Glaucophane-bearing eclogites in the Tso Morari dome (eastern
1188   Ladakh, NW Himalaya). European Journal of Mineralogy, 128(2–3), 197–212.
1189   https://doi.org/10.1127/ejm/9/5/1073

1190   Degeling, H., & Eggins, S. (2001). Zr budgets for metamorphic reactions, and the formation of zircon
1191   from garnet breakdown. Mineralogical Magazine, 65(6), 749–758.
1192   https://doi.org/10.1180/0026461016560006

1193   Ding, H., Zhang, Z., Dong, X., Tian, Z., Xiang, H., Mu, H., Gou, Z., Shui, X., Li, W. & Mao, L. (2016).
1194   Early Eocene (c. 50 Ma) collision of the Indian and Asian continents: Constraints from the
1195   North Himalayan metamorphic rocks, southeastern Tibet. Earth and Planetary Science Letters,
1196   435, 64-73. https://doi.org/10.1016/j.epsl.2015.12.006

1197   Domeier, M. (2016). A plate tectonic scenario for the Iapetus and Rheic oceans. Gondwana Research,
1198   36, 275-295.

1199   Donaldson, D. G., Webb, A. A. G., Menold, C. A., Kylander-Clark, A. R. C., & Hacker, B. R. (2013).
1200   Petrochronology of Himalayan ultrahigh-pressure eclogite. Geology, 41(8), 835–838.
1201   https://doi.org/10.1130/G33699.1

1202   Doubrovine, P.V., Steinberger, B. & Torsvik, T.H. (2012). Absolute plate motions in a reference frame
1203   defined by moving hot spots in the Pacific, Atlantic, and Indian oceans. Journal of Geophysical
1204   Research: Solid Earth, 117. https://doi.org/10.1029/2011JB009072

1205   Dutta, D., & Mukherjee, S. (2021). Extrusion kinematics of UHP terrane in a collisional orogen: EBSD
1206   and microstructure-based approach from the Tso Morari Crystallines (Ladakh Himalaya).
1207   Tectonophysics, 800. https://doi.org/10.1016/j.tecto.2020.228641

1208   Eagles, G. (2019). A little spin in the Indian Ocean plate circuit. Tectonophysics, 754, 80-100.

1209   Epard, J., & Steck, A. (2008). Structural development of the Tso Morari ultra-high pressure nappe of
1210   the   Ladakh   Himalaya.   Tectonophysics,   451(1–4),   242–264.
1211   https://doi.org/10.1016/j.tecto.2007.11.050

1212   Foster, G. and Parrish, R.R., 2003. Metamorphic monazite and the generation of PTt paths. Geological
1213   Society,   London,   Special   Publications, 220(1),   pp.25-47.
1214   https://doi.org/10.1144/GSL.SP.2003.220.01.02

1215   Fuchs, G., & Linner, M. (1996). On the geology of the suture zone and Tso Morari dome in Eastern
1216   Ladakh (Himalaya). Jahrbuch Der Geologischen Bundesanstalt, 139(191), 207.

1217   Gansser, A., 1966. The Indian Ocean and the Himalayas, a geological interpretation: Eclogae Geol.
1218   Eclogae Geol. Helv. 67, 479–507.

1219   Garzanti, E., Radeff, G. & Malusà, M.G. (2018). Slab breakoff: A critical appraisal of a geological
1220   theory as applied in space and time. Earth-Science Reviews, 177, 303-319.

1221   Garzanti, E., & Van Haver, T. (1988). The indus clastics: forearc basin sedimentation in the Ladakh
1222   Himalaya (India). Sedimentary Geology, 59(3–4), 237–249. https://doi.org/10.1016/0037-
1223   0738(88)90078-4

1224   Geisler, T., Schaltegger, U., & Tomaschek, F. (2007). Re-equilibration of Zircon in Aqueous Fluids
1225   and Melts. Elements, 3(1), 43–50. https://doi.org/10.2113/GSELEMENTS.3.1.43

1226   Gibbons, A.D., Zahirovic, S., Müller, R.D., Whittaker, J.M. & Yatheesh, V. (2015). A tectonic model
1227   reconciling evidence for the collisions between India, Eurasia and intra-oceanic arcs of the
1228   central-eastern   Tethys.   Gondwana   Research,   28,   451-492.
1229   https://doi.org/10.1016/j.gr.2015.01.001

1230   Girard, M. (2001). Metamorphism and tectonics of the transition between non metamorphic Tethayan
1231   Himalaya sediments and the North Himalayan Crystalline Zone (Rupshuarea, Ladakh, NW
1232   India).   Section   Des   Sciences   de   La   Terre   de   l'université.

1233   http://www.unil.ch/files/live/sites/iste/files/shared/X.Library/Memoirs of Geology/35 – Girard
1234   (2001).pdf

1235   Girard, M., & Bussy, F. (1999). Late Pan-African magmatism in the Himalaya: new geochronological
1236   and geochemical data from the Ordovician Tso Morari metagranites (Ladakh, NW India).
1237   Schweizerische Mineralogische Und Petrographische Mitteilungen, 79, 399–418.
1238   http://doi.org/10.5169/seals-60215

1239   Gordon, S., Little, T., Hacker, B., Bowring, S., Korchinski, M., Baldwin, S., & Kylander-Clark, A.
1240   (2012). Multi-stage exhumation of young UHP–HP rocks: Timescales of melt crystallization in
1241   the D'Entrecasteaux Islands, southeastern Papua New Guinea. Earth and Planetary Science
1242   Letters, 351, 237–246. https://doi.org/10.1016/j.epsl.2012.07.014

1243   Goscombe, B., Gray, D. & Foster, D.A. (2018). Metamorphic response to collision in the Central
1244   Himalayan   Orogen.   Gondwana   Research,   57,   191-265.
1245   https://doi.org/10.1016/j.gr.2018.02.002

1246   Gilotti, J.A., Jones, K.A., Elvevold, S., Higgins, A.K., Gilotti, J.A. & Smith, M.P. (2008). Caledonian
1247   metamorphic patterns in Greenland. The Greenland Caledonides: Evolution of the Northeast
1248   Margin of Laurentia. Geological Society of America. 202, 0.

1249   Green, O., Searle, M., Corfield, R., & Corfield, R. (2008). Cretaceous-Tertiary carbonate platform
1250   evolution and the age of the India-Asia collision along the Ladakh Himalaya (Northwest India).
1251   The Journal of Geology, 116(4), 331–353. http://www.jstor.org/stable/10.1086/588831

1252   Guan, Q., Zhu, D.-C., Zhao, Z.-D., Dong, G.-C., Zhang, L.-L., Li, X.-W., Liu, M., Mo, X.-X., Liu, Y.-
1253   S. & Yuan, H.-L. (2012). Crustal thickening prior to 38Ma in southern Tibet: Evidence from
1254   lower crust-derived adakitic magmatism in the Gangdese Batholith. Gondwana Research, 21,
1255   88-99. https://doi.org/10.1016/j.gr.2011.07.004

1256   Guillot, S., Hattori, K., Agard, P., Schwartz, S. & Vidal, O. (2009). Exhumation Processes in Oceanic
1257   and Continental Subduction Contexts: A Review. Berlin, Heidelberg. Springer Berlin
1258   Heidelberg, 175-205. https://link.springer.com/chapter/10.1007/978-3-540-87974-9_10

1259   Guillot, S., Mahéo, G., de Sigoyer, J., Hattori, K. H., & Pêcher, A. (2008). Tethyan and Indian
1260   subduction viewed from the Himalayan high- to ultrahigh-pressure metamorphic rocks.
1261   Tectonophysics, 451(1–4), 225–241. https://doi.org/10.1016/j.tecto.2007.11.059

1262   Guillot, S., Sigoyer, J. De, & Lardeaux, J. (1997). Eclogitic metasediments from the Tso Morari area
1263   (Ladakh, Himalaya): Evidence for continental subduction during India-Asia convergence.
1264   Contributions   to   Mineralogy   and   Petrology,   128(2–3),   197–212.
1265   https://doi.org/10.1007/s004100050303

1266   Gürer, D., Granot, R. & van Hinsbergen, D.J.J. (2022). Plate tectonic chain reaction revealed by noise
1267   in the Cretaceous quiet zone. Nature Geoscience, 15, 233-239.

1268   Hacker, B.R., Andersen, T.B., Johnston, S., Kylander-Clark, A.R.C., Peterman, E.M., Walsh, E.O. &
1269   Young, D. (2010). High-temperature deformation during continental-margin subduction &
1270   exhumation: The ultrahigh-pressure Western Gneiss Region of Norway. Tectonophysics, 480,
1271   149-171. https://doi.org/10.1016/j.tecto.2009.08.012

1272   Hacker, B. R., & Gerya, T. V. (2013). Paradigms, new and old, for ultrahigh-pressure tectonism.
1273   Tectonophysics, 603, 79–88. https://doi.org/10.1016/j.tecto.2013.05.026

1274   Hacker, B. R., Gerya, T. V., & Gilotti, J. a. (2013). Formation and exhumation of ultrahigh-pressure
1275   terranes. Elements, 9(4), 289–293. https://doi.org/10.2113/gselements.9.4.289

1276   Hall, R. (2012). Late Jurassic–Cenozoic reconstructions of the Indonesian region and the Indian Ocean.
1277   Tectonophysics, 570-571, 1-41.

1278   Harrison, T.M., Célérier, J., Aikman, A.B., Hermann, J. and Heizler, M.T., (2009). Diffusion of 40Ar
1279   in muscovite. Geochimica et Cosmochimica Acta, 73(4), pp.1039-1051.
1280   https://doi.org/10.1016/j.gca.2008.09.038

1281   Harrison, T.M., Duncan, I.A.N. and Mcdougall, I.A.N., (1985). Diffusion of 40Ar in biotite:
1282   temperature, pressure and compositional effects. Geochimica et Cosmochimica Acta, 49(11),
1283   pp.2461-2468. https://doi.org/10.1016/0016-7037(85)90246-7

1284   Horstwood, M. S., Košler, J., Gehrels, G., Jackson, S. E., McLean, N. M., Paton, C., Pearson, N.J.,
1285   Sircombe, K., Sylvester, P., Vermeesch, P., & Bowring, J. F. (2016). Community-derived
1286   standards for LA-ICP-MS U-(Th-) Pb geochronology–Uncertainty propagation, age
1287   interpretation and data reporting. Geostandards and Geoanalytical Research, 40(3), 311–332.
1288   https://doi.org/10.1111/j.1751-908X.2016.00379.x

1289   Hosseini, K., Matthews, K.J., Sigloch, K., Shephard, G.E., Domeier, M. & Tsekhmistrenko, M. (2018).
1290   SubMachine: Web-Based Tools for Exploring Seismic Tomography and Other Models of
1291   Earth's Deep Interior. Geochemistry, Geophysics, Geosystems, 19, 1464-1483.

1292   Hu, X., Garzanti, E., Moore, T., & Raffi, I. (2015). Direct stratigraphic dating of India-Asia collision
1293   onset at the Selandian (middle Paleocene, 59±1 Ma). Geology,. Geology, 43(10), 859–862.
1294   https://doi.org/10.1130/G36872.1

1295   Hu, X., Garzanti, E., Wang, J., Huang, W., An, W. & Webb, A. (2016). The timing of India-Asia
1296   collision onset – Facts, theories, controversies. Earth-Science Reviews, 160, 264-299.
1297   https://doi.org/10.1016/j.earscirev.2016.07.014

1298 Ingalls, M., Rowley, D.B., Currie, B. & Colman, A.S. (2016). Large-scale subduction of continental
1299   crust implied by India–Asia mass-balance calculation. Nature Geoscience, 9, 848-853.

1300 Jacob, J., Dyment, J. & Yatheesh, V. (2014). Revisiting the structure, age, and evolution of the Wharton
1301   Basin to better understand subduction under Indonesia. Journal of Geophysical Research: Solid
1302   Earth, 119, 169-190.

1303 Jagoutz, O., Bouilhol, P., Schaltegger, U. & Müntener, O. (2019). The isotopic evolution of the
1304   Kohistan Ladakh arc from subduction initiation to continent arc collision. Geological Society,
1305   London, Special Publications, 483, 165-182. https://doi.org/10.1144/SP483.7

1306 Ji, M., Gao, X.-Y., Xia, Q.-X. & Zheng, Y.-F. (2024). Secular change of metamorphic features in the
1307   Himalayan orogen during the Cenozoic and its tectonic implications. Earth-Science Reviews,
1308   248, 104640.

1309 Jonnalagadda, M. K., Karmalkar, N. R., Duraiswami, R. A., Harshe, S., Gain, S., & Griffin, W. L.
1310   (2017). Formation of atoll garnets in the UHP eclogites of the Tso Morari Complex, Ladakh,
1311   Himalaya. Journal of Earth System Science, 126(8), 107. https://doi.org/10.1007/s12040-017-
1312   0887-y

1313 Kaneko, Y., Katayama, I., Yamamoto, H., Misawa, K., Ishikawa, M., Rehman, H. U., Kausar, A. B., &
1314   Shiraishi, K. (2003). Timing of Himalayan ultrahigh-pressure metamorphism: sinking rate and
1315   subduction angle of the Indian continental crust beneath Asia. Journal of Metamorphic
1316   Geology, 21(6), 589–599. https://doi.org/10.1046/j.1525-1314.2003.00466.x

1317 Kapp, P. & DeCelles, P.G. (2019). Mesozoic–Cenozoic geological evolution of the Himalayan-Tibetan
1318   orogen and working tectonic hypotheses. American Journal of Science, 319, 159-254.
1319   https://doi.org/10.2475/03.2019.01

1320 Kohn, M. J., Corrie, S. L., & Markley, C. (2015). The fall and rise of metamorphic zircon. American
1321   Mineralogist, 100(4), 897–908. https://doi.org/10.2138/AM-2015-5064

1322 Kohn, M.J., Engi, M. & Lanari, P. (2017). Petrochronology. Methods and Applications, Mineralogical
1323   Society of America Reviews in Mineralogy and Geochemistry, 83, 575.

1324 Kooijman, E., Mezger, K. and Berndt, J., (2010). Constraints on the U–Pb systematics of metamorphic
1325   rutile from in situ LA-ICP-MS analysis. Earth and Planetary Science Letters, 293(3-4), pp.321-
1326   330.

1327 Konrad-Schmolke, M., O'Brien, P., & Capitani, C. de. (2008). Garnet growth at high-and ultra-high
1328   pressure conditions and the effect of element fractionation on mineral modes and composition.
1329   Lithos, 103(3–4), 309–332. https://doi.org/10.1016/j.lithos.2007.10.007

1330 Kylander-Clark, A. R. C., Hacker, B. R., & Mattinson, J. M. (2008). Slow exhumation of UHP terranes:
1331 Titanite and rutile ages of the Western Gneiss Region, Norway.
1332 https://doi.org/10.1016/j.epsl.2008.05.019

1333 Laik, A., Schellart, W.P. & Strak, V. (2022). Sustained indentation in 2-D models of continental
1334 collision involving whole mantle subduction. Geophysical Journal International, 232, 343-365.

1335 Lamont, T.N., Searle, M.P., Hacker, B.R., Htun, K., Htun, K.M., Morley, C.K., Waters, D.J. & White,
1336 R.W. (2021). Late Eocene-Oligocene granulite facies garnet-sillimanite migmatites from the
1337 Mogok Metamorphic belt, Myanmar, and implications for timing of slip along the Sagaing
1338 Fault. Lithos, 386-387, 106027. https://doi.org/10.1016/j.lithos.2021.106027

1339 Le Fort, P., 1975. Himalayas: the collided range. Present knowledge of the continental arc. Am. J. Sci.
1340 275, 1–44.

1341 Leech, M. L., Singh, S., & Jain, A. K. (2007). Continuous metamorphic zircon growth and interpretation
1342 of U-Pb SHRIMP dating: An example from the Western Himalaya. International Geology
1343 Review, 49(4), 313–328. https://doi.org/10.2747/0020-6814.49.4.313

1344 Li, C., van der Hilst, R. D., Meltzer, A. S., & Engdahl, E. R. (2008). Subduction of the Indian lithosphere
1345 beneath the Tibetan Plateau and Burma. Earth and Planetary Science Letters, 274, 157–168.
1346 https://doi.org/10.1016/j.epsl.2008.07.016Little, T.A., Hacker, B.R., Gordon, S.M., Baldwin,
1347 S.L., Fitzgerald, P.G., Ellis, S. & Korchinski, M. (2011). Diapiric exhumation of Earth's
1348 youngest (UHP) eclogites in the gneiss domes of the D'Entrecasteaux Islands, Papua New
1349 Guinea. Tectonophysics, 510, 39-68. https://doi.org/10.1016/j.tecto.2011.06.006

1350 Long, S.P., Kohn, M.J., Kerswell, B.C., Starnes, J.K., Larson, K.P., Blackford, N.R. & Soignard, E.
1351 (2020). Thermometry and Microstructural Analysis Imply Protracted Extensional Exhumation
1352 of the Tso Morari UHP Nappe, Northwestern Himalaya: Implications for Models of UHP
1353 Exhumation. Tectonics, 39, e2020TC006482. https://doi.org/10.1029/2020TC006482

1354 Lotout, C., Pitra, P., Poujol, M., Anczkiewicz, R. and Van Den Driessche, J., (2018). Timing and
1355 duration of Variscan high-pressure metamorphism in the French Massif Central: A
1356 multimethod geochronological study from the Najac Massif. Lithos, 308, pp.381-394.
1357 https://doi.org/10.1016/j.lithos.2018.03.022

1358 Ma, L., Wang, B.-D., Jiang, Z.-Q., Wang, Q., Li, Z.-X., Wyman, D.A., Zhao, S.-R., Yang, J.-H., Gou,
1359 G.-N. & Guo, H.-F. (2014). Petrogenesis of the Early Eocene adakitic rocks in the Napuri area,
1360 southern Lhasa: Partial melting of thickened lower crust during slab break-off and implications
1361 for crustal thickening in southern Tibet. Lithos, 196-197, 321-338.
1362 https://doi.org/10.1016/j.lithos.2014.02.011

1363   Matthews, K.J., Seton, M. & Müller, R.D. (2012). A global-scale plate reorganization event at
1364   105−100Ma. Earth and Planetary Science Letters, 355-356, 283-298.

1365   Metcalfe, I. (2021). Multiple Tethyan ocean basins and orogenic belts in Asia. Gondwana Research,
1366   100, 87-130.

1367   Mezger, K., Hanson, G., & SR Bohlen. (1989). High-precision UPb ages of metamorphic rutile:
1368   application to the cooling history of high-grade terranes. Earth and Planetary Science Letters,
1369   96(1–2), 106–118. https://doi.org/10.1016/0012-821X(89)90126-X

1370   Möller, C., Andersson, J., Dyck, B., & Antal Lundin, I. (2015). Exhumation of an eclogite terrane as a
1371   hot   migmatitic   nappe,   Sveconorwegian   orogen.   Lithos,   226,   147–168.
1372   https://doi.org/10.1016/J.LITHOS.2014.12.013

1373   Molnar, P. & Stock, J.M. (2009). Slowing of India's convergence with Eurasia since 20 Ma and its
1374   implications   for   Tibetan   mantle   dynamics.   Tectonics,   28.
1375   https://doi.org/10.1029/2008TC002271

1376   Morley, C.K. (2012). Late Cretaceous–Early Palaeogene tectonic development of SE Asia. Earth-
1377   Science Reviews, 115, 37-75.

1378   Mottram, C.M., Cottle, J.M. & Kylander-Clark, A.R.C. (2019). Campaign-style U-Pb titanite
1379   petrochronology: Along-strike variations in timing of metamorphism in the Himalayan
1380   metamorphic   core.   Geoscience   Frontiers,   10,   827-847.
1381   https://doi.org/10.1016/j.gsf.2018.09.007

1382   Müller, R.D., Cannon, J., Qin, X., Watson, R.J., Gurnis, M., Williams, S., Pfaffelmoser, T., Seton, M.,
1383   Russell, S.H.J. & Zahirovic, S. (2018). GPlates: Building a Virtual Earth Through Deep Time.
1384   Geochemistry, Geophysics, Geosystems, 19, 2243-2261.

1385   Müller, R.D., Seton, M., Zahirovic, S., Williams, S.E., Matthews, K.J., Wright, N.M., Shephard, G.E.,
1386   Maloney, K.T., Barnett-Moore, N., Hosseinpour, M., Bower, D.J. & Cannon, J. (2016). Ocean
1387   Basin Evolution and Global-Scale Plate Reorganization Events Since Pangea Breakup. Annual
1388   Review of Earth and Planetary Sciences, 44, 107-138.

1389   Müller, R.D., Zahirovic, S., Williams, S.E., Cannon, J., Seton, M., Bower, D.J., Tetley, M.G., Heine,
1390   C., Le Breton, E., Liu, S., Russell, S.H.J., Yang, T., Leonard, J. & Gurnis, M. (2019). A Global
1391   Plate Model Including Lithospheric Deformation Along Major Rifts and Orogens Since the
1392   Triassic. Tectonics, 38, 1884-1907. https://doi.org/10.1029/2018TC005462

1393   O'Brien, P.J. (2006). The age of deep, steep continental subduction in the NW Himalaya: Relating
1394   zircon growth to metamorphic history. Comment on: "The onset of India–Asia continental

1395   collision: Early, steep subduction required by the timing of UHP metamorphism in the western

1396   . Earth and Planetary Science Letters, 245(3–4), 814–816.

1397   https://doi.org/10.1016/j.epsl.2006.03.033

1398   O'Brien, P.J. (2019a). Eclogites and other high-pressure rocks in the Himalaya: a review. Geological

1399   Society, London, Special Publications, 483, 183-213. https://doi.org/10.1144/SP483.13

1400   O'Brien, P.J., (2019b). Tso Morari coesite eclogite: pseudosection predictions v. the preserved record

1401   and implications for tectonometamorphic models. Geological Society, London, Special

1402   Publications, 474(1), pp.5-24.

1403   O'Brien, P., & Sachan, H. (2000). Diffusion modelling in garnet from Tso Morari eclogite and

1404   implications for exhumation models. Earth Science Frontiers, 7, 25–27.

1405   http://d.wanfangdata.com.cn/periodical_dxqy2000z1010.aspx

1406   O'Brien, P.J., Zotov, N., Law, R.D., Khan, M.A., Jan, M.Q., et al. (2001). Coesite in Himalayan eclogite

1407   and implications for models of India-Asia collision. Geology 29(5): 435-438.

1408   https://doi.org/10.1130/0091-7613(2001)029<0435:CIHEAI>2.0.CO;2

1409   Oriolo, S., Wemmer, K., Oyhantçabal, P., Fossen, H., Schulz, B. and Siegesmund, S., (2018).

1410   Geochronology of shear zones–A review. Earth-Science Reviews, 185, pp.665-683.

1411   https://doi.org/10.1016/j.earscirev.2018.07.007

1412   Palin, R.M., Searle, M.P., St-Onge, M.R., Waters, D.J., Roberts, N.M.W., Horstwood, M.S.A., Parrish,

1413   R.R., Weller, O.M., Chen, S. & Yang, J. (2014). Monazite geochronology and petrology of

1414   kyanite- and sillimanite-grade migmatites from the northwestern flank of the eastern Himalayan

1415   syntaxis. Gondwana Research, 26, 323-347. https://doi.org/10.1016/j.gr.2013.06.022

1416   Palin, R. M., Searle, M. P., Waters, D. J., Horstwood, M. S. A., & Parrish, R. R. (2012). Combined

1417   thermobarometry and geochronology of peraluminous metapelites from the Karakoram

1418   metamorphic complex, North Pakistan; New insight into the tectonothermal evolution of the

1419   Baltoro and Hunza Valley regions. Journal of Metamorphic Geology, 30(8), 793–820.

1420   https://doi.org/10.1111/j.1525-1314.2012.00999.x

1421   Palin, R. M., St-Onge, M. R., Waters, D. J., Searle, M. P., & Dyck, B. (2014). Phase equilibria modelling

1422   of retrograde amphibole and clinozoisite in mafic eclogite from the Tso Morari massif,

1423   northwest India: constraining the P - T - M (H 2 O) conditions of exhumation. Journal of

1424   Metamorphic Geology, 32(7), 675–693. https://doi.org/10.1111/jmg.12085

1425   Parrish, R., Gough, S., Searle, M., & Waters, D. (2006). Plate velocity exhumation of ultrahigh-pressure

1426   eclogites in the Pakistan Himalaya. Geology, 34(11), 989–992.

1427   https://doi.org/10.1130/G22796A.1

1428 Parsons, A.J., Hosseini, K., Palin, R.M. & Sigloch, K. (2020). Geological, geophysical and plate
1429   kinematic constraints for models of the India-Asia collision and the post-Triassic central Tethys
1430   oceans. Earth-Science Reviews, 208, 103084. https://doi.org/10.1016/j.earscirev.2020.103084

1431 Parsons, A.J., Sigloch, K. & Hosseini, K. (2021). Australian Plate Subduction is Responsible for
1432   Northward Motion of the India-Asia Collision Zone and ∼1,000 km Lateral Migration of the
1433   Indian Slab. Geophysical Research Letters, 48, e2021GL094904.
1434   https://doi.org/10.1029/2021GL094904

1435 Passchier, C. W., & Trouw, R. A. J. (2005). Deformation Mechanisms. In Microtectonics (pp. 25–66).
1436   Springer-Verlag. https://doi.org/10.1007/3-540-29359-0_3

1437 Patriat, P. & Achache, J. (1984). India–Eurasia collision chronology has implications for crustal
1438   shortening and driving mechanism of plates. Nature, 311, 615-621.
1439   https://doi.org/10.1038/311615a0

1440 Piazolo, S., Belousova, E., La Fontaine, A., Corcoran, C., & Cairney, J. M. (2017). Trace element
1441   homogeneity from micron- to atomic scale: Implication for the suitability of the zircon GJ-1 as
1442   a trace element reference material. Chemical Geology, 456, 10–18.
1443   https://doi.org/10.1016/J.CHEMGEO.2017.03.001

1444

1445 Regis, D., Warren, C.J., Mottram, C.M. and Roberts, N.M., (2016). Using monazite and zircon
1446   petrochronology to constrain the P–T–t evolution of the middle crust in the Bhutan Himalaya.
1447   Journal of Metamorphic Geology, 34(6), pp.617-639. https://doi.org/10.1111/jmg.12196

1448 Replumaz, A., Capitanio, F.A., Guillot, S., Negredo, A.M., Villaseñor, A., 2014. The coupling of Indian
1449   subduction and Asian continental tectonics. Gondwana Res. 26, 608–626.
1450   https://doi.org/10.1016/j.gr.2014.04.003

1451 Roberts, N. M., Thomas, R. J., & Jacobs, J. (2016). Geochronological constraints on the metamorphic
1452   sole of the Semail ophiolite in the United Arab Emirates. Geoscience Frontiers, 7(4), 609–619.
1453   https://doi.org/10.1016/j.gsf.2015.12.003

1454 Rubatto, D. (2002). Zircon trace element geochemistry: partitioning with garnet and the link between
1455   U–Pb ages and metamorphism. Chemical Geology, 184(1), 123–138.
1456   https://doi.org/10.1016/S0009-2541(01)00355-2

1457 Rubatto, D., & Hermann, J. (2003). Zircon formation during fluid circulation in eclogites (Monviso,
1458   Western Alps): Implications for Zr and Hf budget in subduction zones. Geochimica et
1459   Cosmochimica Acta, 67(12), 2173–2187. https://doi.org/10.1016/S0016-7037(02)01321-2

1460 Rubatto, D., Müntener, O., Barnhoorn, A., & Gregory, C. (2008). Dissolution-reprecipitation of zircon
1461   at low-temperature, high-pressure conditions (Lanzo Massif, Italy). American Mineralogist,
1462   93(10), 1519–1529. https://doi.org/10.2138/AM.2008.2874

1463 Sachan, H. K., Mukherjee, B. K., Ogasawara, Y., Maruyama, S., Ishida, H., Muko, A., & Yoshioka, N.
1464   (2004). Discovery of coesite from Indus Suture Zone (ISZ), Ladakh, India: Evidence for deep
1465   subduction. European Journal of Mineralogy, 16(2), 235–240. https://doi.org/10.1127/0935-
1466   1221/2004/0016-0235

1467 Schaltegger, U., Fanning, C. M., Günther, D., Maurin, J. C., Schulmann, K., & Gebauer, D. (1999).
1468   Growth, annealing and recrystallization of zircon and preservation of monazite in high-grade
1469   metamorphism: Conventional and in-situ U-Pb isotope, cathodoluminescence and
1470   microchemical evidence. Contributions to Mineralogy and Petrology, 134(2–3), 186–201.
1471   https://doi.org/10.1007/s004100050478

1472 Schlup, M., & Carter, A. (2003). Exhumation history of eastern Ladakh revealed by 40Ar/39Ar and
1473   fission-track ages: the Indus River–Tso Morari transect, NW Himalaya. Journal of the
1474   Geological Society, 3, 385–399. https://doi.org/10.1144/0016-764902-084

1475 Schwartz, S., Lardeaux, J. M., Tricart, P., Guillot, S., & Labrin, E. (2007). Diachronous exhumation of
1476   HP–LT metamorphic rocks from south-western Alps: evidence from fission-track analysis.
1477   Terra Nova, 19(2), 133–140. https://doi.org/10.1111/J.1365-3121.2006.00728.X

1478 Searle, M.P. (2019). Timing of subduction initiation, arc formation, ophiolite obduction and India–Asia
1479   collision in the Himalaya. Geological Society, London, Special Publications, 483, 19-37.
1480   https://doi.org/10.1144/SP483.8

1481 Searle, M.P., Elliott, J.R., Phillips, R.J. & Chung, S.-L. (2011). Crustal–lithospheric structure and
1482   continental extrusion of Tibet. Journal of the Geological Society, 168, 633-672.
1483   https://doi.org/10.1144/0016-76492010-139

1484 Searle, M.P., Garber, J.M., Hacker, B.R., Htun, K., Gardiner, N.J., Waters, D.J. & Robb, L.J. (2020).
1485   Timing of Syenite-Charnockite Magmatism and Ruby and Sapphire Metamorphism in the
1486   Mogok Valley Region, Myanmar. Tectonics, 39, e2019TC005998.
1487   https://doi.org/10.1029/2019TC005998

1488 Searle, M.P., Morley, C.K., Waters, D.J., Gardiner, N.J., Htun, U.K., Nu, T.T. & Robb, L.J. (2017).
1489   Chapter 12   Tectonic and metamorphic evolution of the Mogok Metamorphic and Jade Mines
1490   belts and ophiolitic terranes of Burma (Myanmar). Geological Society, London, Memoirs, 48,
1491   261-293. http://doi.org/10.1144/M48.12

1492   Searle, M.P., Noble, S.R., Cottle, J.M., Waters, D.J., Mitchell, A.H.G., Hlaing, T. & Horstwood, M.S.A.
1493   (2007). Tectonic evolution of the Mogok metamorphic belt, Burma (Myanmar) constrained by
1494   U-Th-Pb dating of metamorphic and magmatic rocks. Tectonics, 26.
1495   https://doi.org/10.1029/2006TC002083

1496   Sinha Roy, S., 1976. A possible Himalayan microcontinent. Nature 263, 117–120.
1497   https://doi.org/10.1038/263117a0

1498   Skuzovatov, S. Y., Shatsky, V. S., Ragozin, A. L., & Wang, K. L. (2021). Ubiquitous post-peak zircon
1499   in an eclogite from the Kumdy-Kol, Kokchetav UHP-HP Massif (Kazakhstan): Significance of
1500   exhumation-related zircon growth and modification in continental-subduction settings. Island
1501   Arc, 30(1), e12385. https://doi.org/10.1111/IAR.12385

1502   Smit, M.A., Hacker, B.R. & Lee, J. (2014). Tibetan garnet records early Eocene initiation of thickening
1503   in the Himalaya. Geology, 42, 591-594. https://doi.org/10.1130/G35524.1

1504   Smyth, H.R., Hall, R., Nichols, G.J., Draut, A.E., Clift, P.D. & Scholl, D.W. (2008). Cenozoic volcanic
1505   arc history of East Java, Indonesia: The stratigraphic record of eruptions on an active
1506   continental margin. Formation and Applications of the Sedimentary Record in Arc Collision
1507   Zones. Geological Society of America. 436, 0. https://doi.org/10.1130/2008.2436(10)

1508   Soret, M., Larson, K.P., Cottle, J. & Ali, A. (2021). How Himalayan collision stems from subduction.
1509   Geology, 49, 894-898.Sheng, Y. M., Zheng, Y. F., Chen, R. X., Li, Q., & Dai, M. (2012). Fluid
1510   action on zircon growth and recrystallization during quartz veining within UHP eclogite:
1511   Insights from U–Pb ages, O–Hf isotopes and trace elements. Lithos, 136–139, 126–144.
1512   https://doi.org/10.1016/J.LITHOS.2011.06.012

1513   Steck, A., Epard, J. L., Vannay, J. C., Hunziker, J., Girard, M., Morard, A., & Robyr, M. (1998).
1514   Geological transect across the Tso Morari and Spiti areas: The nappe structures of the Tethys
1515   Himalaya. Eclogae Geologicae Helvetiae, 91, 103–121. Stampfli, G.M., Borel, G.D., 2004. The
1516   TRANSMED transects in space and time: constraints on the paleotectonic evolution of the
1517   Mediterranean domain. In: Cavazza, W., Roure, F., Spakman, W., Stampfli, G.M., Ziegler, P.A.
1518   (Eds.), The TRANSMED Atlas. The Mediterranean Region from Crust to Mantle: Geological
1519   and Geophysical Framework of the Mediterranean and the Surrounding Areas. Springer, Berlin
1520   Heidel-berg, pp. 53–80. https://doi.org/10.1007/978-3-642-18919-7_3

1521   St-Onge, M. R., Rayner, N., Palin, R. M., Searle, M. P., & Waters, D. J. (2013). Integrated pressure –
1522   temperature – time constraints for the Tso Morari dome (Northwest India): implications for
1523   the burial and exhumation path of UHP units in the western Himalaya. Journal of Metamorphic
1524   Geology, 31(5), 469–504. https://doi.org/10.1111/jmg.12030

1525 Tapster, S., Condon, D. J., Naden, J., Noble, S. R., Petterson, M. G., Roberts, N. M. W., Saunders, A.
1526   D., & Smith, D. J. (2016). Rapid thermal rejuvenation of high-crystallinity magma linked to
1527   porphyry copper deposit formation; evidence from the Koloula Porphyry Prospect, Solomon
1528   Islands. Earth and Planetary Science Letters, 442, 206–217.
1529   https://doi.org/10.1016/J.EPSL.2016.02.046

1530 Tomaschek, F., Kennedy, A. K., Villa, I. M., Lagos, M., & Ballhaus, C. (2003). Zircons from Syros,
1531   Cyclades, Greece—Recrystallization and Mobilization of Zircon During High-Pressure
1532   Metamorphism. Journal of Petrology, 44(11), 1977–2002.
1533   https://doi.org/10.1093/PETROLOGY/EGG067

1534 Torsvik, T.H., Amundsen, H., Hartz, E.H., Corfu, F., Kusznir, N., Gaina, C., Doubrovine, P.V.,
1535   Steinberger, B., Ashwal, L.D. & Jamtveit, B. (2013). A Precambrian microcontinent in the
1536   Indian Ocean. Nature Geoscience, 6, 223-227.

1537 Torsvik, T.H., Müller, R.D., Van der Voo, R., Steinberger, B. & Gaina, C. (2008). Global plate motion
1538   frames: Toward a unified model. Reviews of Geophysics, 46.
1539   https://doi.org/10.1029/2007RG000227

1540 Tual, L., Smit, M.A., Kooijman, E., Kielman-Schmitt, M. and Ratschbacher, L., (2022). Garnet, zircon,
1541   and monazite age and REE signatures in (ultra) high-temperature and high-pressure rocks:
1542   Examples from the Caledonides and the Pamir. Journal of Metamorphic Geology, 40(8),
1543   pp.1321-1346. https://doi.org/10.1111/jmg.12667

1544 van de Lagemaat, S.H.A. & van Hinsbergen, D.J.J. 2024. Plate tectonic cross-roads: Reconstructing the
1545   Panthalassa-Neotethys Junction Region from Philippine Sea Plate and Australasian oceans and
1546   orogens. Gondwana Research, 126, 129-201.

1547 van Hinsbergen, D.J.J., Lippert, P.C., Li, S., Huang, W., Advokaat, E.L. & Spakman, W. (2019).
1548   Reconstructing Greater India: Paleogeographic, kinematic, and geodynamic perspectives.
1549   Tectonophysics, 760, 69-94. https://doi.org/10.1016/j.tecto.2018.04.006

1550 Vavra, G., Gebauer, D., Schmid, R., & Compston, W. (1996). Multiple zircon growth and
1551   recrystallization during polyphase Late Carboniferous to Triassic metamorphism in granulites
1552   of the Ivrea Zone (Southern Alps): an ion microprobe (SHRIMP) study. Contributions to
1553   Mineralogy and Petrology 1995 122:4, 122(4), 337–358.
1554   https://doi.org/10.1007/S004100050132

1555 Vermeesch, P. (2018). IsoplotR: A free and open toolbox for geochronology. Geoscience Frontiers,
1556   9(5), 1479–1493. https://doi.org/10.1016/J.GSF.2018.04.001

1557   Vry, J., & Baker, J. (2006). LA-MC-ICPMS Pb–Pb dating of rutile from slowly cooled granulites:
1558   confirmation of the high closure temperature for Pb diffusion in rutile. Geochimica et
1559   Cosmochimica Acta, 70(7), 1807–1820. https://doi.org/10.1016/j.gca.2005.12.006

1560   Warnock, A.C., Zeitler, P.K., Wolf, R.A. and Bergman, S.C., (1997). An evaluation of low-temperature
1561   apatite UTh/He thermochronometry. Geochimica et Cosmochimica Acta, 61(24), pp.5371-
1562   5377. https://doi.org/10.1016/S0016-7037(97)00302-5

1563   Warren, C J. (2013). Exhumation of (ultra-)high-pressure terranes: concepts and mechanisms. Solid
1564   Earth, 4, 75–92. https://doi.org/10.5194/se-4-75-2013

1565   Warren, C. J., Beaumont, C., & Jamieson, R. A. (2008a). Formation and exhumation of ultra-high-
1566   pressure rocks during continental collision: Role of detachment in the subduction channel.
1567   Geochemistry, Geophysics, Geosystems, 9, Q04019. https://doi.org/10.1029/2007GC001839

1568   Warren, C.J., Beaumont, C., & Jamieson, R. A. (2008b). Modelling tectonic styles and ultra-high
1569   pressure (UHP) rock exhumation during the transition from oceanic subduction to continental
1570   collision.   In   Earth   and   Planetary   Science   Letters,   267(1).
1571   https://doi.org/10.1016/j.epsl.2007.11.025

1572   Warren, Clare J., Beaumont, C., & Jamieson, R. A. (2008c). Deep subduction and rapid exhumation:
1573   Role of crustal strength and strain weakening in continental subduction and ultrahigh-pressure
1574   rock exhumation. Tectonics, 27(6), n/a-n/a. https://doi.org/10.1029/2008TC002292

1575   Warren, C. J., Beaumont, C., Jamieson, R. A., & Lee, B. (2007). Detachment and Exhumation of Ultra-
1576   high-pressure Rocks During Continental Subduction. American Geophysical Union, Fall
1577   Meeting 2007, Abstract #V44A-01.

1578   Waters, D.J. (2019). Metamorphic constraints on the tectonic evolution of the High Himalaya in Nepal:
1579   the art of the possible. Geological Society, London, Special Publications, 483, 325-375.
1580   https://doi.org/10.1144/SP483-2018-187

1581   Watson, E., Wark, D. and Thomas, J. (2006) Crystallization thermometers for zircon and rutile,
1582   Contributions to Mineralogy and Petrology, 151(4), p. 413. https://doi.org/10.1007/s00410-
1583   006-0068-5

1584   Weller, O. M., St-Onge, M. R., Rayner, N., Waters, D. J., Searle, M. P., & Palin, R. M. (2016). U–Pb
1585   zircon geochronology and phase equilibria modelling of a mafic eclogite from the Sumdo
1586   complex of south-east Tibet: Insights into prograde zircon growth and the assembly of the
1587   Tibetan plateau. Lithos, 262, 729–741. https://doi.org/10.1016/J.LITHOS.2016.06.005

1588 Wilke, F., O'Brien, P., Gerdes, A., Tinnerman, M., Sudo, M., & Khan, M. (2010). The multistage
1589   exhumation history of the Kaghan Valley UHP series, NW Himalaya, Pakistan from U-Pb and
1590   40Ar/39Ar ages. European Journal of Mineralogy, 22(5), 703–719.
1591   https://doi.org/10.1127/0935-1221/2010/0022-2051

1592 Wilke, F., O'Brien, P., Schmidt, A., & Ziemann, M. (2015). Subduction, peak and multi-stage
1593   exhumation metamorphism: Traces from one coesite-bearing eclogite, Tso Morari, western
1594   Himalaya. Lithos, 231, 77–91. https://doi.org/10.1016/j.lithos.2015.06.007

1595 Wu, Y. B., Zheng, Y. F., Zhao, Z. F., Gong, B., Liu, X., & Wu, F. Y. (2006). U–Pb, Hf and O isotope
1596   evidence for two episodes of fluid-assisted zircon growth in marble-hosted eclogites from the
1597   Dabie orogen. Geochimica et Cosmochimica Acta, 70(14), 3743–3761.
1598   https://doi.org/10.1016/J.GCA.2006.05.011

1599 Xia, Q. X., Zheng, Y. F., Yuan, H., & Wu, F. Y. (2009). Contrasting Lu–Hf and U–Th–Pb isotope
1600   systematics between metamorphic growth and recrystallization of zircon from eclogite-facies
1601   metagranites in the Dabie orogen, China. Lithos, 112(3–4), 477–496.
1602   https://doi.org/10.1016/J.LITHOS.2009.04.015

1603 Yamato, P., Burov, E., Agard, P., Le Pourhiet, L. & Jolivet, L. (2008). HP-UHP exhumation during
1604   slow continental subduction: Self-consistent thermodynamically and thermomechanically
1605   coupled model with application to the Western Alps. Earth and Planetary Science Letters, 271,
1606   63-74. https://doi.org/10.1016/j.epsl.2008.03.049

1607 Yan, H., Xu, Z., Long, X., Li, J., Shu, C., Gou, L. & Wu, B. (2023). Transition from non-adakitic rocks
1608   to adakitic rocks in the southern Lhasa subterrane: Implications for progressive crustal
1609   thickening and tectonic evolution during the Early Cenozoic. Journal of Asian Earth Sciences,
1610   105995.

1611 Zack, T. and Kooijman, E., (2017). Petrology and geochronology of rutile. Reviews in Mineralogy and
1612   Geochemistry, 83(1), pp.443-467. https://doi.org/10.2138/rmg.2017.83.14

1613 Zahirovic, S., Matthews, K.J., Flament, N., Müller, R.D., Hill, K.C., Seton, M. & Gurnis, M. (2016).
1614   Tectonic evolution and deep mantle structure of the eastern Tethys since the latest Jurassic.
1615   Earth-Science Reviews, 162, 293-337.

1616 Zhang, D., Ding, L., Chen, Y., Schertl, H.-P., Qasim, M., Jadoon, U. K., et al. (2022). Two contrasting
1617   exhumation scenarios of deeply subducted continental crust in north Pakistan. Geochemistry,
1618   Geophysics, Geosystems, 23, e2021GC010193. https://doi.org/10.1029/2021GC010193

1619 Zhang, Z.M., Zhao, G.C., Santosh, M., Wang, J.L., Dong, X. & Liou, J.G. (2010). Two stages of
1620   granulite facies metamorphism in the eastern Himalayan syntaxis, south Tibet: petrology,

1621   zircon geochronology and implications for the subduction of Neo-Tethys and the Indian

1622   continent beneath Asia. Journal of Metamorphic Geology, 28, 719-733.

1623   https://doi.org/10.1111/j.1525-1314.2010.00885.x

1624   Zhou, J., Su, H., 2019. Site and timing of substantial India-Asia collision inferred from crustal volume

1625   budget. Tectonics 38, 2275–2290. https://doi.org/10.1029/2018TC005412

1626   Zhu, D.-C., Wang, Q., Chung, S.-L., Cawood, P.A. & Zhao, Z.-D. (2019). Gangdese magmatism in

1627   southern Tibet and India–Asia convergence since 120 Ma. Geological Society, London, Special

1628   Publications, 483, 583-604. https://doi.org/10.1144/SP483.14

Table 1. Published geochronology results from Tso Morari, Kaghan and Stak. Sample numbers not available designated as n/a. Also shown in Figure 8.

Rock type	Sample number	Age (Ma)	Mineral	Method	Interpretation	Reference
			Tso Morari			
Retrogressed eclogite	CM71710-4	45.3±1.6	Zircon	U-Pb	Eclogite facies	Donaldson et al. (2013)
Retrogressed eclogite	DD71710-2b	44.2±1.2	Zircon	U-Pb	Eclogite facies	Donaldson et al. (2013)
Retrogressed eclogite	L08-03A	58.0 ± 2.2	Zircon	U-Pb shrimp	Prograde	St-Onge et al (2013)
Retrogressed eclogite	L08-03A	50.8 ± 1	Zircon	U-Pb shrimp	UHP	St-Onge et al (2013)
Puga gneiss	L08-03E/F	45.3 ± 1.1	Monazite	Th-Pb shrimp	Amphibolite facies	St-Onge et al (2013)
Puga gneiss	L08-03E/F	43.3 ± 1.1	Allanite	U-Pb shrimp	Amphibolite facies	St-Onge et al (2013)
Granite gneiss	T18, T38	53.3 ± 0.7	Zircon	U-Pb shrimp	UHP	Leech et al (2007)
Granite gneiss	T18, T38	50.1 ± 0.6	Zircon	U-Pb shrimp	Eclogite facies	Leech et al (2007)
Granite gneiss	T18, T38	47 ± 0.5	Zircon	U-Pb shrimp	Amphibolite facies	Leech et al (2007)
Granite gneiss	T18, T38	45.2 ± 0.7	Zircon	U-Pb shrimp	Amphibolite facies	Leech et al (2007)
Puga gneiss	n/a	51.1 ± 0.1	Biotite	Ar/Ar	<300°c	Schlup and Carter (2003)
Metapelite	n/a	14.1 ± 1.3	Apatite	Fission track	<120°c	Schlup and Carter (2003)
Metapelite	n/a	34-45 ± 2	Zircon	Fission track	<120°c	Schlup and Carter (2003)
Puga gneiss	n/a	7.5 ± 3	Apatite	Fission track	<120°c	Schlup and Carter (2003)
Puga gneiss	n/a	13.2-16.4 ± 3	Apatite	Fission track	<120°c	Schlup and Carter (2003)
Puga gneiss	n/a	21-23.4 ± 3	Apatite	Fission track	<120°c	Schlup and Carter (2003)
Retrogressed eclogite	Ch157a	55 ± 7	Grt-Gln-WR	Sm/Nd	Eclogite facies	De Sigoyer et al (2000)
Amphibolite	Ts34	55 ± 12	Grt-Cpx-WR	Lu/Hf	Eclogite facies	De Sigoyer et al (2000)
Metapelite	n/a	55 ± 17	Allanite	U-Pb	Eclogite facies	De Sigoyer et al (1999)
Retrogressed eclogite	Ts45	47 ± 11	Grt-Gln-WR	Sm/Nd	Amphibolite facies	De Sigoyer et al (2000)
Metapelite	Ch165	48 ± 2	Phengite	Ar/Ar	Amphibolite facies	De Sigoyer et al (2000)
Metapelite	Ch223	45 ± 4.4	Phe-Ap-WR	Rb/Sr	Amphibolite facies	De Sigoyer et al (2000)
Metapelite	Lk93-42/40	31.1 ± 0.3	Muscovite	Ar/Ar	<300°c	De Sigoyer et al (2000)
Metapelite	Lk93-42/40	29 ± 0.4	Biotite	Ar/Ar	<300°c	De Sigoyer et al (2000)
Metapelite	Lk93-42/40	29.3 ± 0.3	Biotite	Ar/Ar	<300°c	De Sigoyer et al (2000)
Granite	As9660	479 ± 2	Zircon	U-Pb	Igneous	Girard and Bussy (1999)
Puga gneiss	G9628	479 ± 2	Zircon	U-Pb	Igneous	Girard and Bussy (1999)
Rupshu granite	V9692	482.5 ± 1	Zircon	U-Pb	Igneous	Girard and Bussy (1999)
			Kaghan valley			
Retrogressed eclogite	Kv4	46.4 ± 0.1	Zircon	U-Pb ID-TIMS	Eclogite facies	Parrish et al., (2006)
Granite gneiss	Kv16	45.5 ± 6.6	Zircon	U-Pb ID-TIMS	Eclogite facies	Parrish et al., (2006)
Granite gneiss	Kv16	46.5 ± 1.0	Allanite	U-Pb ID-TIMS	Eclogite facies	Parrish et al., (2006)
Retrogressed eclogite	2016PK39 and 2016PK43-2	46 ± 2.0 Ma	Zircon	U-Pb SIMS	Eclogite facies	Zhang et al., (2022)
Granite gneiss	Kv16	44-46.4	Titanite	U-Pb ID-TIMS	Amphibolite facies	Parrish et al., (2006)
Eclogite	n/a	44.1	Rutile	U-Pb ID-TIMS	Amphibolite facies	Treloar et al. (2003)
Retrogressed eclogite	n/a	46.2 ± 0.7	Zircon	U-Pb shrimp	Eclogite facies	Kaneko et al., (2003)
Orthogneiss	H65 and H37	47 to 39 ± 1.0	Titanite	LA-SS-ICP-MS	Amphibolite facies	Soret et al., (2020)
Gneiss	K4-119	47.3 ± 0.3	Phengite	Ar/Ar	Eclogite facies	Wilke et al. (2010)
Gneiss	K3-26	47.3 ± 0.4	Zircon	U-Pb LA-ICP-MS	Eclogite facies	Wilke et al. (2010)
Retrogressed eclogite	K4-99	46.6 ± 0.5	Amphibole	Ar/Ar	Amphibolite facies	Wilke et al. (2010)
Retrogressed eclogite	K4-60	44.1 ± 0.3	Rutile	U-Pb LA-ICP-MS	Amphibolite facies	Wilke et al. (2010)
	K4-71	41.3 ± 4.7	Titanite	U-Pb LA-ICP-MS	Amphibolite facies	Wilke et al. (2010)
Gneiss	K4-97	34.5 ± 0.2	Phengite	Ar/Ar	Amphibolite facies	Wilke et al. (2010)
Gneiss	K4-21	28.1 ± 0.2	Biotite	Ar/Ar	Amphibolite facies	Wilke et al. (2010)
Gneiss	K4-99	23.6 ± 0.1	Biotite	Ar/Ar	Amphibolite facies	Wilke et al. (2010)
Gneiss	K4-37	21.7 ± 0.2	Biotite	Ar/Ar	Amphibolite facies	Wilke et al. (2010)
			Stak massif			
Retrogressed eclogite	n/a	51.3 ± 0.7 and 60.4 ± 0.6	Zircon	U-Pb shrimp	Eclogite facies	Riel et al., (2008)